Annual Report

Development of Advanced Electrochemical Emission Spectroscopy for Monitoring Corrosion in Simulated DOE Liquid Waste

by

Digby D. Macdonald, Sue Liu, Elizbieta Sikora, and Jun Liu
Center for Electrochemical Science and Technology
Pennsylvania State University
University Park, PA 16802
ddm2@psu.edu

Submitted to

Department of Energy Environmental Science Program

Grant No. DE-FG07-97ER62515 (Project 60219)

January 20 2002

Executive Summary

The current report summarizes work performed on the project over the past calendar year (2001). The work concentrated on four areas: the fracture of AISI 4340 steel simulating weld heat-affected zones in DOE liquid waste storage tanks, investigation of the passive state on nickel, which is commonly used for containing highly alkaline solutions, development of a new theory for the transient growth of passive films on metals in contact with aqueous solutions, and exploration of the passive state on iron, because it is passivity that allows iron-based alloys to be used to contain DOE's liquid waste.

Fracture of AISI 4340 steel in concentrated sodium hydroxide solution has been monitored by measuring the coupling current that flows between the crack and the external surfaces. The results clearly demonstrate that positive current flows from the crack to the external cathodes (through the solution) during crack growth of AISI 4340 steel in concentrated (6 to12 M) sodium hydroxide solution at 70 ^{o}C. The (electron) coupling current contains periodic noise that is attributed to fracture events occurring at the crack front, with the amplitude of the noise and the mean current increasing with crack growth rate. The characteristic shape of the individual transients in the noise at lower SCC crack growth rate is a rapid drop followed by slow recovery. The form of the noise in the coupling current during SCC at high NaOH concentration (8 M and 12 M) is attributed to overlap of many cracks propagating simultaneously through micro fracture events along grain boundaries. The discrete events, which have a dimension of about 49 μm, are postulated to be hydrogen induced, and the mechanism of caustic cracking of AISI 4340 steel is considered to be hydrogen embrittlement along grain boundaries. Measurement of the electrochemical noise is shown to be capable of detecting and distinguishing between uniform corrosion and stress corrosion cracking in the steel/NaOH system. The coupling current data are consistent with a hydrogen embrittlement mechanism for crack advance.

The passive film formed anodically on nickel in borate buffer solution in both the passive and transpassive regions is found to be p-type, corresponding to a preponderance of metal vacancies (over oxygen vacancies and nickel interstitials) in the barrier layer. However, at high anodic potentials, some n-type character was detected by Mott-Schottky analysis, which is probably due to the presence of free charge carriers (electrons) from the evolution of oxygen and or the oxidative ejection of Ni^{3+} at the barrier layer/outer layer interface. The p-type character of the film is consistent with the diagnostic criteria obtained from the Point Defect Model for a passive film, in which the majority defect in the NiO barrier layer is the metal vacancy. The transpassive state is postulated to comprise a thick, porous oxide film on the surface, with the current probably being due to the oxidative ejection of Ni^{3+} species from the barrier layer and oxygen evolution within the pores, or both.

A new rate law for the growth of anodic passive films on metal surfaces is derived from the Point Defect Model (PDM). The model recognizes both the growth of the barrier oxide layer into the metal via the generation of oxygen vacancies at the metal/film interface and the dissolution of the barrier layer at the film/solution interface. The new rate law accounts for the existence of a steady state in film thickness, as well as for the transients in thickness and film growth current as the potential is stepped in the positive or negative direction from an initial steady state. The predictions of the PDM, with respect to the thickness of the barrier layer, are

compared with those of the High Field Model. It is shown that the latter cannot account for the existence of steady states or the decrease in barrier layer thickness on stepping the potential in the negative direction. The predicted transients in film thickness and growth current density are found to be in good fidelity with the measured transients on tungsten in pH = 1.5 phosphate buffer solution as the voltage is cycled between 10 V_{sce} and 6 V_{sce}. Finally, the new rate law accounts for passive film thinning under negative potential step conditions as the pH is changed over the range of 1.5 to 5.1 and as the initial and final voltages are changed in a systematic manner, such that the voltage excursion is constant.

The passive state on iron in EDTA (Ethylene Diammine Tetraacetic Acid, disodium salt)-containing borate buffer solutions of pH = 8.4 to 10.0 at ambient temperature has been explored using potentiodynamic polarization and steady state techniques, including Mott-Schottky (MS) analysis. EDTA effectively suppresses the formation of the outer layer of the passive film thereby rendering the barrier layer amenable to direct examination. It is shown that the barrier layer on iron is a highly disordered, n-type semiconductor. The barrier layer thickness varies linearly with applied potential, whereas the steady state current density does not depend on the formation voltage. EDTA present in the solution renders the barrier layer of the passive film more defective, as indicated by MS analysis, and the donor density decreases with increasing film formation potential. These findings suggest that the dominant defects in the barrier layer are oxygen vacancies or cation interstitials, or both. No evidence of cation vacancies, which would render the barrier layer p-type and would impart a voltage dependence to the steady state current was obtained. Thus, if cation vacancies are present, they are not the dominant defect.

TABLE OF CONTENTS

CHAPTER 1: Fracture of AISI 4340 Steel in Concentrated Sodium Hydroxide Solution 6

1.1: Abstract. 6

1.2: Introduction. 6

1.3: Experimental Procedure. 8
- a. Materials and specimens. 8
- b. Loading apparatus. 9
- c. Environment. 9
- d. Electrochemical emission measurements. 10

1.4: Results. 10
- a. 12 M NaOH Solution. 10
- b. 8 M NaOH Solution. 15
- c. 6 M NaOH Solution. 16
- d. 5 M and 1 M NaOH Solutions. 19

1.5: Discussion. 20

1.6: Summary. 22

1.7: References. 22

CHAPTER 2: Nature of the Passive Film on Nickel. 24

2.1: Abstract. 24

2.2: Introduction. 24

2.3: Experimental. 25

2.4: Results and Discussion. 25
- a. Impedance measurements. 28
- b. Capacitance measurements. 30

2.5: Summary and Conclusions. 33

2.6: References. 34

CHAPTER 3: New Rate Laws for the Growth and Reduction of Passive Films. 35

3.1: Abstract. 35

3.2: Introduction. 35

3.3: Theory. 36
- a. Transient in Film Thickness. 38
- b. Transient in Film Growth Current 39

3.4: Discussion. 39

3.5: Summary and Conclusions. 46
3.6: References. 46

CHAPTER 4: The Passivity of Iron in the Presence of EDTA. Part II: The Defect and Electronic Structures of the Barrier Layer. 48

4.1: Abstract. 48
4.2: Introduction. 48
4.3: Experimental. 50
4.4: Results and Discussion. 51
4.5: Summary and Conclusions. 58
4.6: References. 59

Chapter 1

FRACTURE OF AISI 4340 STEEL IN CONCENTRATED SODIUM HYDROXIDE SOLUTION

1.1: ABSTRACT

Fracture of AISI 4340 steel in concentrated sodium hydroxide solution has been monitored by measuring the coupling current that flows between the crack and the external surfaces. The results clearly demonstrate that positive current flows from the crack to the external cathodes (through the solution) during crack growth of AISI 4340 steel in concentrated (6 to12 M) sodium hydroxide solution at 70 ^{o}C. The (electron) coupling current contains periodic noise that is attributed to fracture events occurring at the crack front, with the amplitude of the noise and the mean current increasing with crack growth rate. The characteristic shape of the individual transients in the noise at lower SCC crack growth rate is a rapid drop followed by slow recovery. The form of the noise in the coupling current during SCC at high NaOH concentration (8 M and 12 M) is attributed to overlap of many cracks propagating simultaneously through micro fracture events along grain boundaries. The discrete events, which have a dimension of about 49 μm, are postulated to be hydrogen induced, and the mechanism of caustic cracking of AISI 4340 steel is considered to be hydrogen embrittlement along grain boundaries. Measurement of the electrochemical noise is shown to be capable of detecting and distinguishing between uniform corrosion and stress corrosion cracking in the steel/NaOH system. The coupling current data are consistent with a hydrogen embrittlement mechanism for crack advance.

1.2: INTRODUCTION

The US Department of Energy (DOE) currently stores about 253 million liters of high-level nuclear waste at the Hanford Reservation in the State of Washington[1]. The waste consists mainly of concentrated solutions of sodium nitrate, sodium hydroxide, and sodium nitrite, with a high pH (>12 at 25 ^{o}C), and is stored in a variety of single walled and doubled wall tanks manufactured from ASTM A537-Cl. 1, ASTM A515-Gr. 60, or ASTM A516-Gr. 60 steel[1]. The single walled tanks were not stress relieved after welding, and hence contain weld heat-affected zones (HAZs) that are partially martensitic. These HAZs are susceptible to stress corrosion cracking (SCC) and/or hydrogen-induced cracking (HIC). Some of the single walled tanks are suspected to be leaking, due to corrosion-induced penetrations of the walls.

Accordingly, failure by caustic cracking of the carbon steel storage tank must be considered as one of the principal threats to tank integrity. An enormous literature exists on the environment-assisted cracking (EAC) of carbon steels in caustic solutions, but the work is almost entirely phenomenological in nature. For example, it is not always clear whether crack propagation occurs via anodic dissolution or hydrogen-induced fracture, or a combination of both, but the bulk of the evidence suggests that HIC is the fracture mechanism. Thus, it has long been observed that cracks propagate via discrete events and this is often taken as being indicative of the role of hydrogen[2]. Thus, hydrogen is postulated to produce a brittle matrix at the crack tip that undergoes periodic fracture to produce intermittent crack advance[2]. Hydrogen induced cracking occurs with a fracture dimension that is determined by the time between events and the

diffusion length of hydrogen in the matrix (typically a few microns). Stress corrosion cracking (SCC) may also occur by cyclical slip/dissolution/repassivation[3,4] and hence exhibits periodic advance, but the slip dimension is of the order of some low multiple of the Burger's vector (a few nanometers) and is unlikely to give rise to the abrupt transient in current that has been found in this study (see later). Thus, from a mechanistic viewpoint, knowledge of the dimension of the fracture event is most important, for it may provide a means of differentiating between anodic dissolution and hydrogen-induced fracture. However, quantitative knowledge of the mechanism(s) of caustic cracking of carbon steel in highly concentrated alkaline solutions is quite poor. Therefore, emphasis in this part of our work is on the fundamental aspect of caustic cracking mechanisms by using electrochemical emission spectroscopy (EES) on the coupling current that flows between the crack and the external surfaces to ascertain the dimension of the brittle micro fracture events that occur during crack propagation. In order to carry out the study in a parametric manner, we have employed the simple $NaOH/H_2O$ electrolyte systems. A high strength, low alloy steel (AISI 4340) was chosen for the test material and was heat-treated to represent the heat-affected zones adjacent to welds in DOE storage tanks.

Methods are currently being developed in our laboratory to measure the electrochemical emissions in the coupling current from growing cracks in high strength, low alloy steel. These techniques are expected to provide fundamental information on the mechanisms of crack propagation. The method that is being currently employed is to measure the coupling current that flows between the crack and the external surface, as a crack propagates through the steel (Figure 1.1).

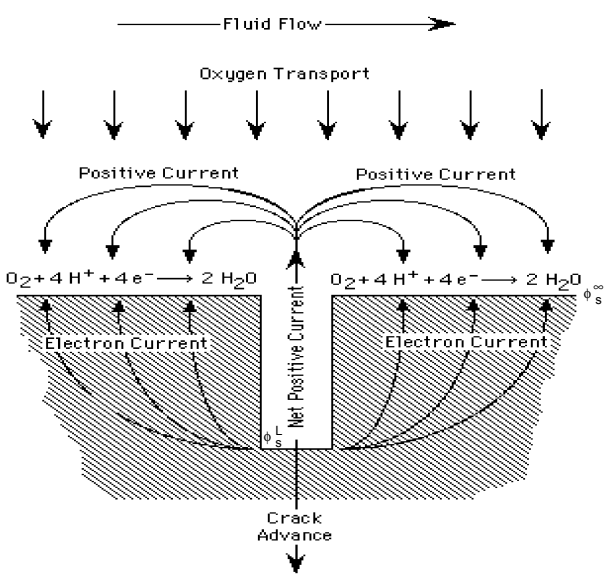

Figure 1.1. Schematic of the origin of the coupling current in stress corrosion cracking. The coupling current is required by the differential aeration hypothesis for localized corrosion and the conservation of charge requires that the electron current flowing through the substrate from the crack to the external surface must be equal to the positive ionic current flowing through the solution from the crack to the external surface.

A coupling current of appropriate magnitude is required by the differential aeration hypothesis to satisfy charge conservation in the system [5]. Previous work on stress corrosion cracking in Type 304 SS in high temperature aqueous systems shows that the noise in the coupling current can be attributed to brittle micro fracture events that have a dimension of the order of 3 μm and that these fracture events occur in "packages" of 4 to 13 corresponding to the grain size of the steel[2]. The present work seeks to determine whether similar events can be detected in the coupling current that is produced in the fracture of high strength, low alloy steels in simulated DOE waste environments. Detection and characterization of the noise in the coupling current is expected to provide mechanistic information of unprecedented value.

1.3: EXPERIMENTAL PROCEDURE

Materials and specimens

The material used in this investigation was a commercial heat of AISI 4340 (UNS G43400) steel, which was prepared by electric furnace melting and vacuum degassing. The chemical composition is given in Table 1.1. The as-received steel plate was 1.5 inches thick. The plate was first cut into blanks and heat-treated according to the procedures given in Table 1.2. The yield strength was not measured, but the value was estimated to be about 1490 MPa according to the measured hardness (48.5 R_c) and the typical properties of AISI 4340 steel of this temper. Specimens were machined in the fully heat treated condition.

Table 1.1
Chemical Composition of AISI 4340 Steel

Element	C	Mn	P	S	Si	Cu	Ni	Cr	Mo	V
Wt. %	0.43	0.71	0.013	0.004	0.26	0.18	1.72	0.80	0.24	0.59

Table 1.2
Heat Treatment and Mechanical Properties of AISI 4340 Steel

Heat Treatment	Normalization	1659 F (889 °C)	1 hour Air cool
	Austenization	1550 F (843 °C)	1 hour Oil quench
	Temper	700 F (371 °C)	1 hour Air cool
Mechanical Properties	Hardness, Rc :	48.5	
	Yield Strength:	1490 MPa (estimated)	

The configuration employed for monitoring the coupling current during crack propagation in the compact tension [C(T)] specimen is shown in Figure 1.2. The specimen geometry conforms to ASTM E399 based upon W = 2.997-cm (1.18 inches). All specimens were prepared in the short transverse-longitudinal (S-L) orientation. Shallow side grooves (5% of the specimen thickness on both sides) were machined along the crack plane to enhance plane strain and to guide the direction of the growing crack. The effect of reduced thickness (B_n) on the stress intensity was taken into account by replacing B by $(BB_n)^{1/2}$ in the equation for K_I, where B is the specimen thickness and B_n is the reduced thickness at the groove[6].

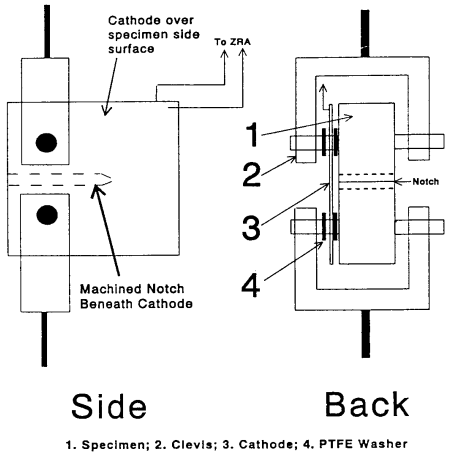

Figure 1.2. Specimen configuration used in detecting and measuring the coupling current flowing from a crack to the external metal surface. Note that the C(T) fracture mechanics specimen is coated with PTFE to inhibit the cathodic reduction of oxygen on the specimen surface. Instead, the current flows from the crack to the side cathodes (only one shown) where it is consumed by O_2 reduction. The electron current flows from the crack tip to the side cathodes via a zero resistance ammeter, which is used for its measurement

The specimens were carefully cleaned and wires were then spot-welded onto the surface. Then, the entire surface of each specimen was coated with baked-on polytetrafluoroethylene (PTFE) for electrical insulation, so that only the crack after fatigue precracking was exposed to the environment. The side cathodes were then mounted and held in place by insulated clips.

Loading apparatus

An H-shape loading frame and a special tank and clevis made of Inconel 600 alloy were used for conducting SCC experiments in hot, concentrated sodium hydroxide solution. Prior to stress corrosion cracking, the C(T) specimens were pre-cracked to total crack length of 0.40~0.42 W as per ASTM E399 guidelines for load and load shedding at a frequency of 20Hz. After initiating and propagating the fatigue crack for about 1mm under K_{max}=20 MPa$\sqrt{m}$ with R=0.1, the maximum applied stress intensity was reduced to less than 10 ksi$\sqrt{in}$ (11MPa$\sqrt{m}$), in order to yield a sharp crack and to minimize the size of the plastic zone ahead of the crack tip. The precracked C(T) specimen was loaded by an oil-driven ram, with the load being measured using a sensitive load cell. The crack mouth opening displacement (CMOD) of the C(T) specimen was measured using a sensitive LVDT and the crack length was evaluated from the CMOD and load, as per ASTM E399.

Environment

Our experiments were carried out at the open circuit potential in various (1 to12 M) NaOH solutions, which were prepared from reagent grade sodium hydroxide and deionized water. The solution was contained in an alkali-resistant vessel fitted with a reflux condenser. The solution was not deaerated and the dissolved oxygen concentration was approximately

8ppm. Heating was achieved by a heating tape wrapped around the outside the vessel. The test temperature (70 °C) was measured by a PTFE coated thermocouple and was controlled to within ±1 °C using a proportional temperature controller.

Electrochemical emission measurements

Stress corrosion cracking is a typical localized corrosion process that falls within the differential aeration (DA) hypothesis, which requires the spatial separation of the anode and the cathode for crack propagation to proceed. In a DA system with solution of high conductivity, the local anode exists in the region of the system that has the least access to the cathodic depolarizer (i.e., at the crack tip), while the local cathode(s) occurs on those regions that have the greatest access to the depolarizer (external surfaces or at least the entrance region to the crack). Thus, as the crack propagates, the electrons that are released at the crack tip flow through the metal to the external surface, where they are consumed by the reduction of cathodic depolarizer(s) present in the solution (Fig. 1.1). Accordingly, the internal crack environment is strongly "coupled" to the external surfaces. The magnitude of the current, and hence the crack growth rate, is constrained by the conservation of charge, which is the basis of various "coupled environment" models that have been developed by this group over the past decade[5] to describe corrosion cavity growth.

The (electron) coupling current (Figure 1.1) was monitored using a zero-resistance ammeter (ZRA), as shown schematically in Figure 1.2. Two plate cathodes were mounted on either side of the electrically insulated, precracked CT specimen. The cathodes were made of AISI 1010 (UNS G10100) carbon steel, which has a similar chemical composition to AISI 4340 steel. Inserting the ZRA between the sample and the cathodes in this circuit permitted measurement of the coupling current produced during crack extension. Since the distance over which positive current can travel, as it exits the crack mouth, is limited by the conductivity of solution, the cathodes were placed on the sides of the CT specimen in close proximity to the intersection of the crack plane with the surface. The potential of the specimen was also measured with respect to a platinum electrode by using a high impedance voltmeter. The platinum pseudo reference electrode was placed 2mm from the crack tip on one side of the specimen.

A computer-based data acquisition system with a fast, multi-channel A/D converter and a large buffer was used to record the current and potential vs. time at a sampling frequency of 2 Hz. A Fast Fourier Transform (FFT) algorithm was employed to transform data from the time domain into the frequency domain, in order that periodic components in the (electron) coupling current could be detected and identified. The load and LVDT outputs were also recorded by this system.

After each fracture experiment, the fracture surfaces were examined by scanning electron microscopy (SEM).

1.4: RESULTS

12 M NaOH Solution.

After stabilizing the temperature of the caustic solution at 70 °C, the specimen was loaded to 454 kg (1000 pounds), corresponding to an initial stress intensity factor (K_I) of 13 MPa$\sqrt{m}$ (12 ksi$\sqrt{in}$). Figure 1.3 shows the crack length from the loading line as a function of time after loading was applied. The potential and the (electron) coupling current were recorded

over the time period from 10 minutes before load application to final fracture, which was due to mechanical overload, as shown in Figure 1.4.

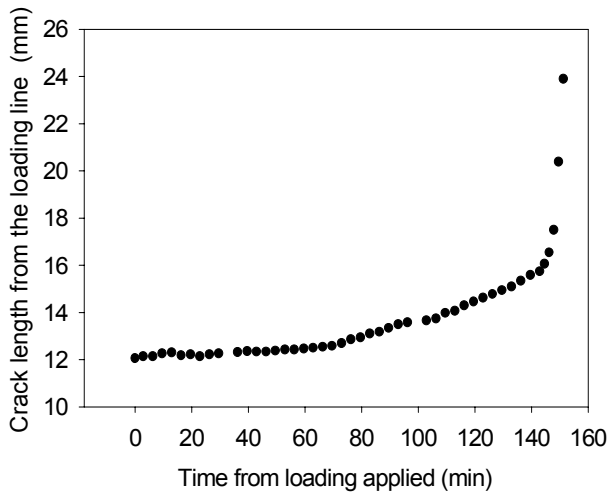

Figure 1.3. The crack length from the loading line vs. time after loading was applied to the AISI 4340 steel C(T) specimen in 12 M sodium hydroxide solution at 70 °C.

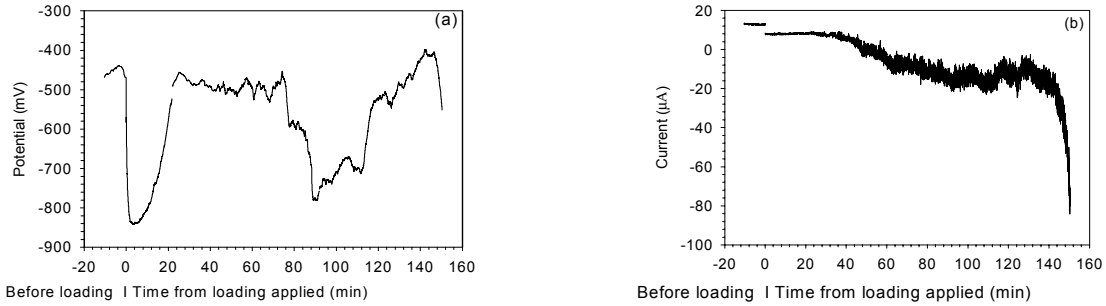

Figure 1.4. Specimen potential (a) and (electron) coupling current (b) versus time for fracture in AISI 4340 steel in 12 M sodium hydroxide solution at 70 ^{o}C.

Small random fluctuations in the (electron) coupling current have been shown to be characteristic of uniform corrosion, and indeed this was the pattern that was observed before the load was applied to the specimen [Figures 1.4(b) and 1.5(a)]. Prior to loading, the (electron) coupling current was found to have a positive sign, corresponding to the flow of electrons through the metal from the cathodes to the specimen. This is most likely due to a small galvanic effect arising from the fact that the cathodes and the specimen are fabricated from slightly different materials. However, upon loading, the (electron) coupling current that flows between

the specimen and the cathode first decreased to a lower value and eventually became negative, corresponding to electron flow from the specimen to the cathodes (or positive ion flow from the crack through the solution to the cathode surfaces) [Figure 1.4(b)]. Thus, during the first stage of the experiment (first 70 minutes after loading), the crack propagates at a very low growth rate, which is dictated by the existence of a residual compressive stress zone ahead of the tip of the fatigue precrack. During this period, the (electron) coupling current changes from positive to negative and the amplitude of the current fluctuations increases gradually with increasing crack length [Figures 1.4(b) and 1.5(b)]. During the second stage of the experiment (from 70 to 142 minutes), the crack growth rate is about 8.3×10^{-5} cm/s (3 mm/hour), which is significantly larger than that observed during the first stage (1.7×10^{-5} cm/s). The (electron) coupling current and the fluctuation amplitude (~10 μA) remain almost constant, as shown in Figures 1.5 (c) and (d). During the final stage of fracture (after 142 minutes), the crack propagates rapidly, ultimately resulting in complete fracture by mechanical overload. The amplitude of the electron current noise increases to 20 μA during the final stage [Figure 1.5(d)], which is twice that observed during the second stage of the experiment.

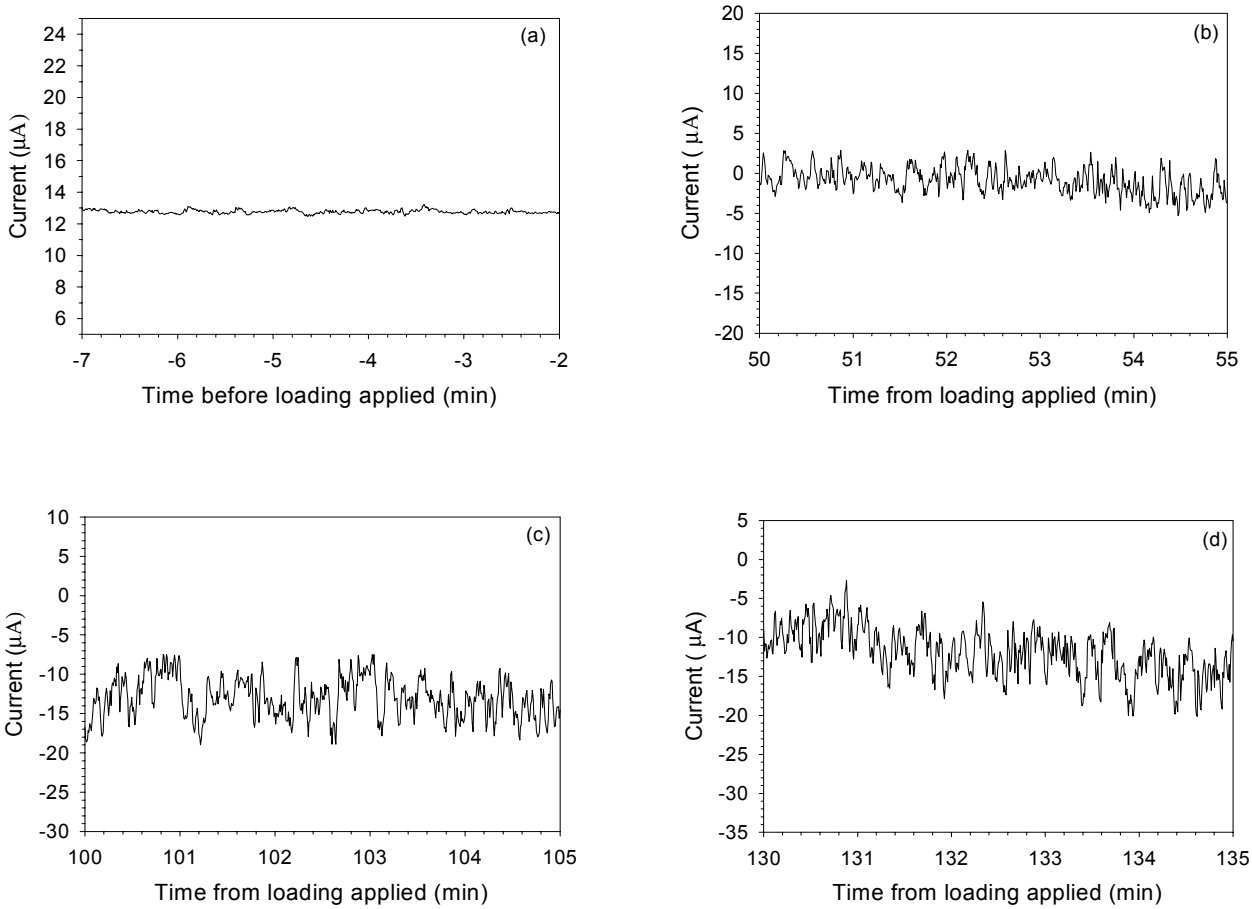

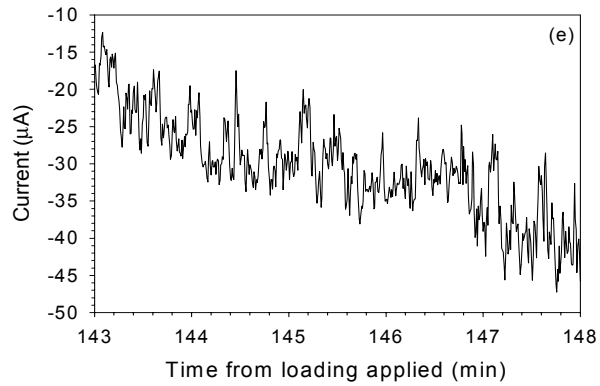

Figure 1.5. Details of the electron current noise at various stages in the fracture history. Before loading (a) and after loading application (b, c, d and e) in 12 M sodium hydroxide solution at 70 °C.

The observations summarized above confirm, in a qualitative manner, that the magnitude of the (electron) coupling current reflects the rate of crack propagation, a finding that is in concert with that of our previous work on crack propagation in sensitized Type 304 SS in high temperature aqueous solutions[2]. The new observation from the present work is that the amplitude of the noise may also be related to the crack propagation rate.

The potential is found to shift in the negative direction promptly upon application of the load, but then recovers gradually as the load is maintained [Figure 1.4(a)]. This transition is probably related to the opening of the fatigue pre-crack, such that the freshly fractured surfaces of the fatigue precrack are exposed to the solution. The potential of the specimen then shifts in the negative direction as the growth rate increases at the beginning of the second stage, and then recovers (shifts in the positive direction) due to re-passivation as the crack is opened towards final fracture due to the increasing stress intensity. During the final stage, both the (electron) coupling current and the potential shift sharply in the negative direction simultaneously (Figure 1.4), because of the large fresh surface that is exposed to the solution by fast fracture due to mechanical overload. It is postulated that the potential measured here is actually the mixed potential between the CT specimen and the cathodes, rather than the potential at the (emergent) crack tip. This is because the reference electrode was located near the emergent crack tip on one side of specimen, but was also near a cathode that was connected to the specimen through the ZRA.

The data reported here clearly demonstrate that the positive current flows through the solution from the crack tip to the external cathode during crack propagation in AISI 4340 steel in concentrated sodium hydroxide solution at 70 °C. Accordingly, these data confirm that the cathodic reaction is not restricted to the flanks of the crack or to the crack mouth, but that it also occurs on the external surfaces, as postulated in the CEFM model[5]. The magnitude of the (electron) coupling current and the amplitude of the current noise increase with increasing crack growth rate. Finally, periodic pulses in the (electron) coupling current recorded during crack propagation show that caustic-cracking advances by discrete microscopic fracture events, as discussed below.

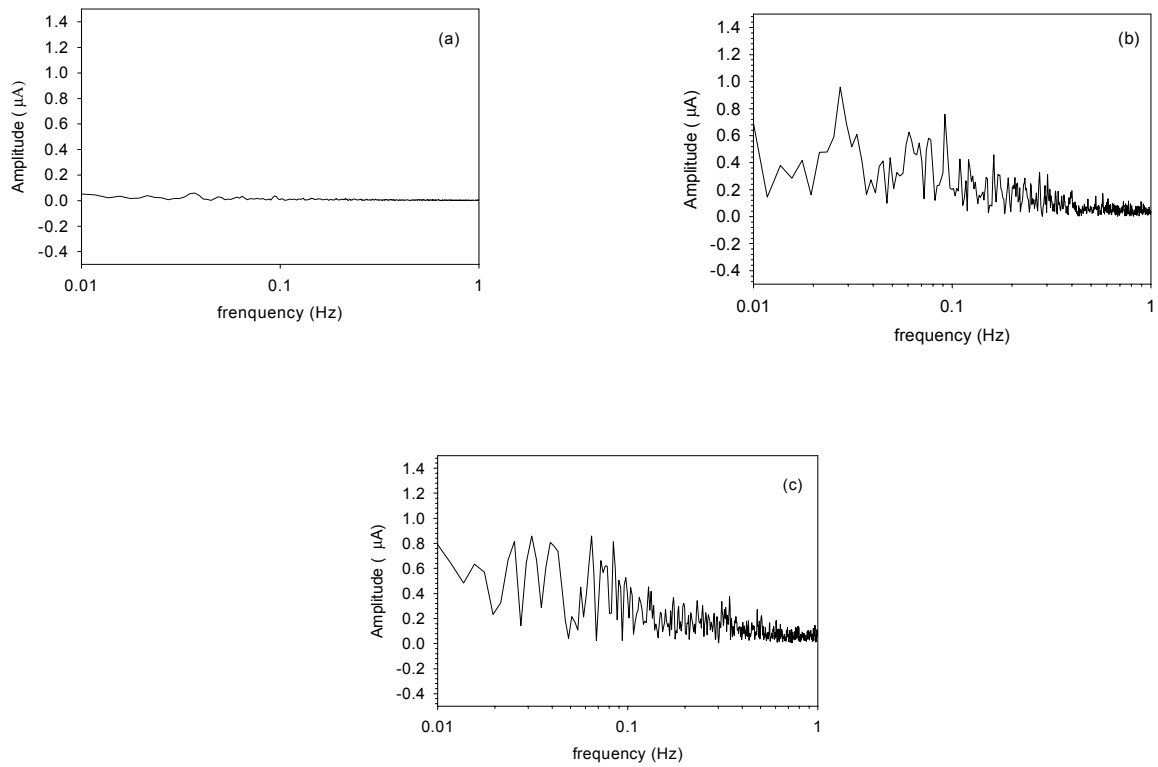

Figure 1.6. Amplitude vs. frequency after FFT transformation of the (electron) coupling current for AISI 4340 steel in 12 M NaOH solution at 70 °C. (a) Before loading application; (b) during the second stage of fracture; and (c) before final fracture of the specimen.

Figure 1.6 shows an amplitude spectrum that was obtained by transforming the (electron) coupling current from the time domain into the frequency domain by using the Fast Fourier Transform (FFT). The results indicate that the event spacing in frequency space increases while, simultaneously, the amplitude decreases with increasing frequency. This is consistent with crack advance via many small micro fracture events, characterized by small current amplitudes, occurring more-or-less simultaneously, superimposed upon less frequent, but larger discrete events of higher current amplitude. The latter events apparently occur at frequencies between 0.02 and 0.1 Hz, as shown in Figures 1.6 (b) and (c). The apparent transients at frequencies below 0.02 Hz are considered to arise from DC drift and hence may be artifacts. Before the application of the load, there are no micro fracture events, and the corresponding (electron) current amplitudes at various frequencies are very small [Figure 1.6 (a)] and are characteristic of general corrosion.

Examination of the fracture surface by optical microscopy shows brittle morphological characteristics. The stress corrosion crack remains in the original pre-crack plane with no tendency for macro crack branching. Fractographic studies of the cleaned surface show that the crack propagation path in caustic solution is typical of intergranular fracture [right part in Figure

1.7 (a)] following the transition zone, which is characterized by mixed intergranular/transgranular morphology near the front of the fatigue pre-crack [left part in Figure 1.7 (a)]. The final fracture zone is predominantly dimpled rupture [Figure 1.7 (b)], which is characteristic of mechanical overload.

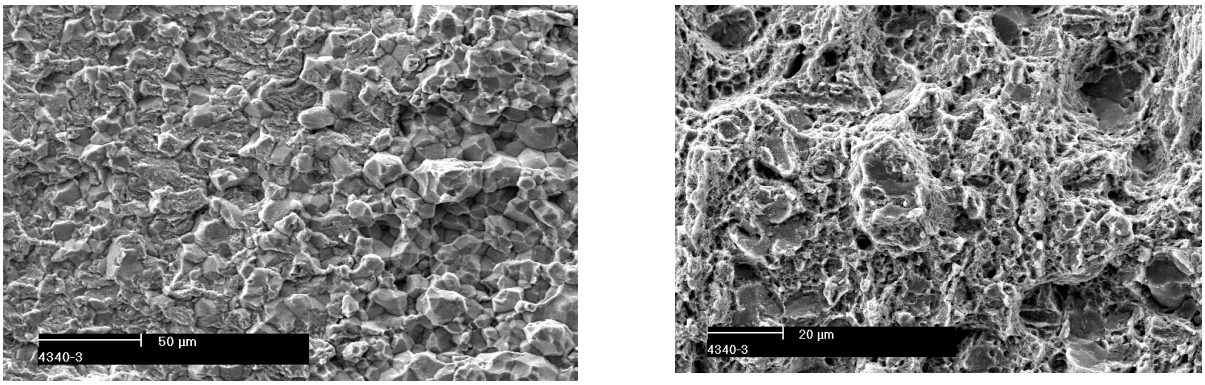

(a) (b)

Subcritical crack growth

Figure 1.7. SEM fractographs of SCC fracture surfaces produced at the free corrosion potential in 12 M NaOH solution at 70 °C. (a) Crack propagating from the fatigue pre-crack front (left) in mixed form to caustic cracking (right) in intergranular form. (b) The final fracture zone showing predominantly dimpled rupture (mechanical overload).

8 M NaOH Solution.

The previous experiment in 12 M NaOH solution postulated that the complicated, quasi-periodic pulses in the (electron) coupling current that occur during SCC is consistent with the overlap of several local cracks propagating simultaneously through micro fracture events. The purpose in choosing a lower NaOH concentration was to reduce the SCC susceptibility, and hence to slow down the crack growth rate, in order to observe individual micro events.

The specimen was loaded to 907 kg (2000 pounds) in 8 M NaOH solution, corresponding to an initial stress intensity factor of 25 MPa$\sqrt{m}$ (23 ksi$\sqrt{in}$) after the temperature of the solution had stabilized at 70 °C. The specimen fractured after 5.5 hours from load application. Figure 1.8 shows the crack length from the loading line vs. time. Figure 1.9 shows the (electron) coupling current before and after the load was applied to the AISI 4340 steel CT specimen in 8 M NaOH solution at 70 °C.

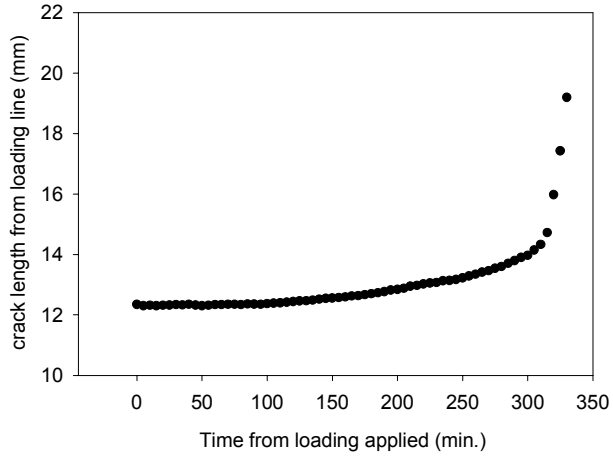

Figure 1.8. The crack length from the loading line vs. time after loading for the AISI 4340 steel C(T) specimen in 8 M NaOH solution at 70 °C.

The results from the experiment in the 8 M NaOH solution are similar to those obtained in the 12 M NaOH solution. Although the crack growth rate in the 8 M NaOH solution is about 4 times lower (during the second stage) than that in 12 M NaOH solution, it is still too high to observe the individual micro-fracture events during crack propagation.

6 M NaOH Solution

In this experiment, the specimen was loaded to 998 kg (2200 pounds) corresponding to an initial stress intensity factor of 27.4 MPa$\sqrt{m}$ (25 ksi$\sqrt{in}$). Low amplitude, random fluctuations in the (electron) coupling current were observed prior to loading, as shown in Figure 1.10. Which are characteristic of uniform corrosion as stated previously. The (electron) coupling current is displaced in the negative direction promptly upon load application, but then recovers gradually to almost the same level, and has the same fluctuation characteristics, as that observed before loading. This transition is attributed to the exposure and subsequent passivation of the surfaces of the fatigue pre-crack to the solution upon the initial application of the load. The noise in the (electron) coupling current recorded during the subsequent 3 hours period from loading shows no obvious change, except for a small DC drift.

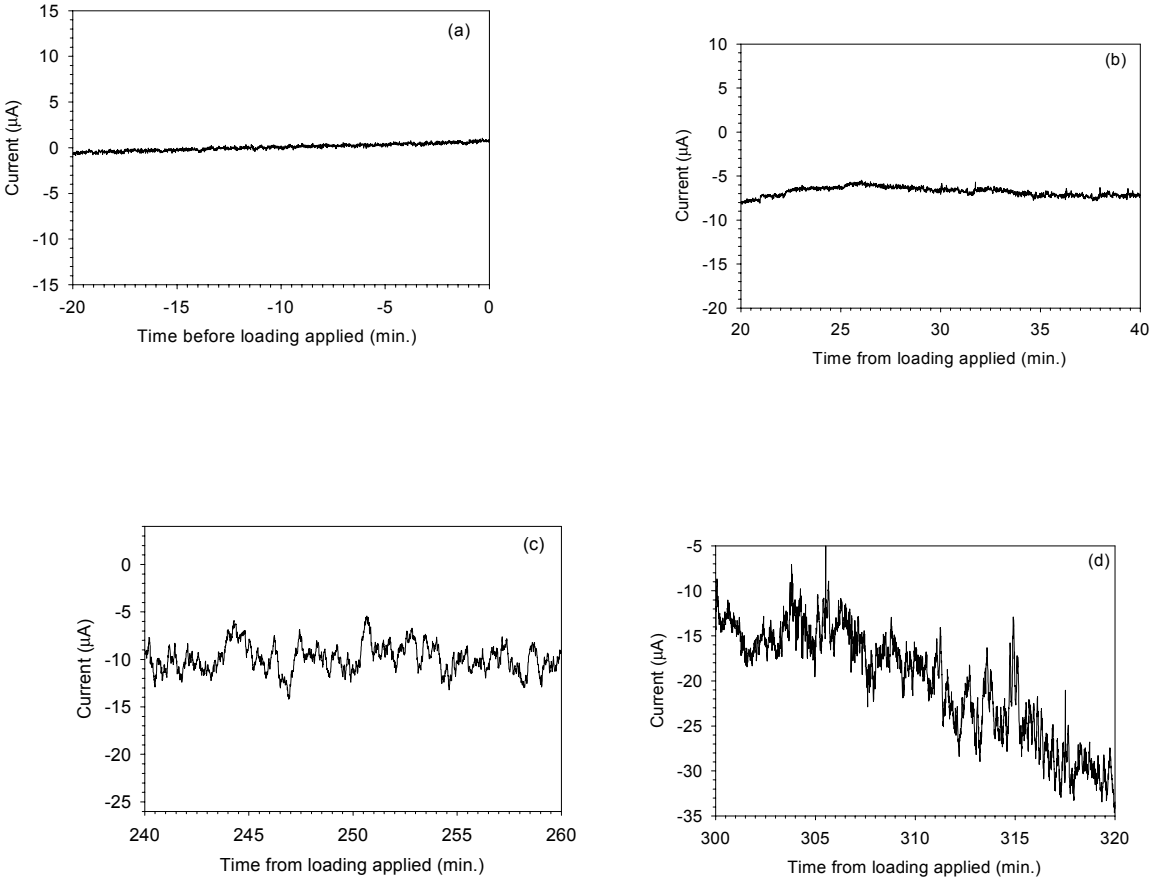

Figure 1.9. The (electron) coupling current before (a) and after (b,c,d) load application to a C(T) specimen of AISI 4340 steel in 8 M NaOH solution at 70 °C.

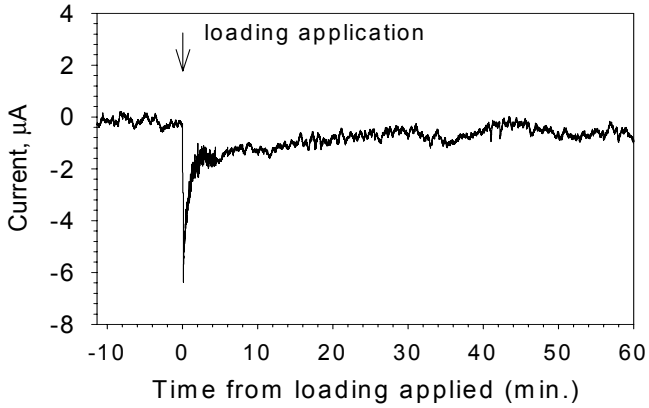

Figure 1.10. The (electron) coupling current vs. time before and after load application in 6 M NaOH at 70 °C.

Four hours later, a significant transient was observed in the (electron) coupling current. Typical data collected after 4 hours from load application are shown in Figure 1.11. Data similar to those shown in Figure 1.11 were also collected from 5 to 52 hours after application of the load. In general, the (electron) coupling current contains individual, low frequency transients with amplitudes ranging from 1.5 to 7 μA. A typical pattern in the current noise is shown in Figure 1.12. The transient in the (electron) coupling current is again characterized by a rapid drop and slow recovery. This type of noise in the (electron) coupling current appears to be quite characteristic of caustic SCC crack propagation.

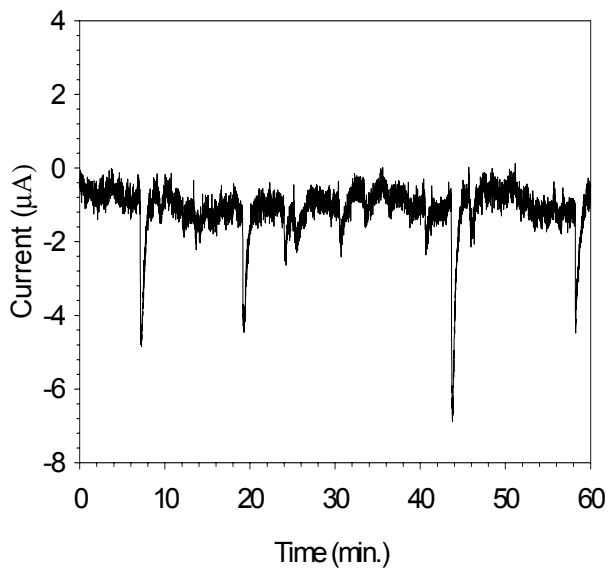

Figure 1.11. Typical transients in the (electron) coupling current from 5 to 52 hours after load application for AISI 4340 steel in 6 M NaOH solution at 70 °C.

The crack propagated for about 100 μm in length in intergranular form (observed by SEM) within the 52-hour observation period after loading. The average crack growth rate was 5.3×10^{-8} cm/s. The results show that temporally resolved brittle micro fracture events can be observed during caustic SCC, provided that the crack growth rate is sufficiently low. Interestingly, the crack growth rate in Type 304 SS in high temperature (250 °C) water[2] discussed earlier in this paper was about 3×10^{-7} cm/s, or about seven times higher than that observed here. In both cases, the quantity CGR/f, where CGR is the crack growth rate and f is the frequency of transients, is similar (~1.5 to 5×10^{-7} cm), suggesting that the micro fracture dimensions are also similar.

5 M and 1 M NaOH Solutions

An experiment was performed in 5 M NaOH solution at 70 °C, in order to reduce the crack growth rate still further, and hence to characterize the current noise at even lower crack growth rate. The specimen was loaded to 499 kg (1100 pounds), corresponding to an initial

stress intensity factor of 14 MPa$\sqrt{m}$ (13 ksi$\sqrt{in}$). After 24 hours, no crack propagation was observed via the LVDT. The load was then increased to 1134 kg (2500 pounds), corresponding to $K_{I,initial}$ = 32 MPa$\sqrt{m}$ (29 ksi$\sqrt{in}$). The LVDT output was then monitored for 24 hours, and still no crack propagation was observed. The (electron) coupling current noise was found to consist of random fluctuations of low amplitude, and no significant difference was observed in the form of the noise before and after application in the load, as shown in Figure 1.13. These results indicate that the K_{ISCC} value for AISI 4340 in 5 M NaOH solution at 70 °C is higher than 32 MPa$\sqrt{m}$ (29 ksi$\sqrt{in}$). Finally, an experiment performed in 1 M NaOH solution under similar loading conditions (32 MPa$\sqrt{m}$) showed no EAC, a finding that is similar to that for the 5 M NaOH solution.

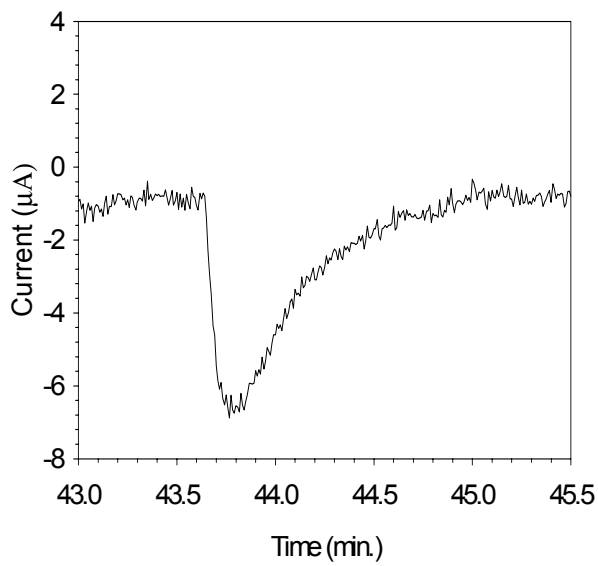

Figure 1.12. Typical transient in the (electron) coupling current for a single fracture event in AISI 4340 steel in 6 M NaOH solution at 70 °C.

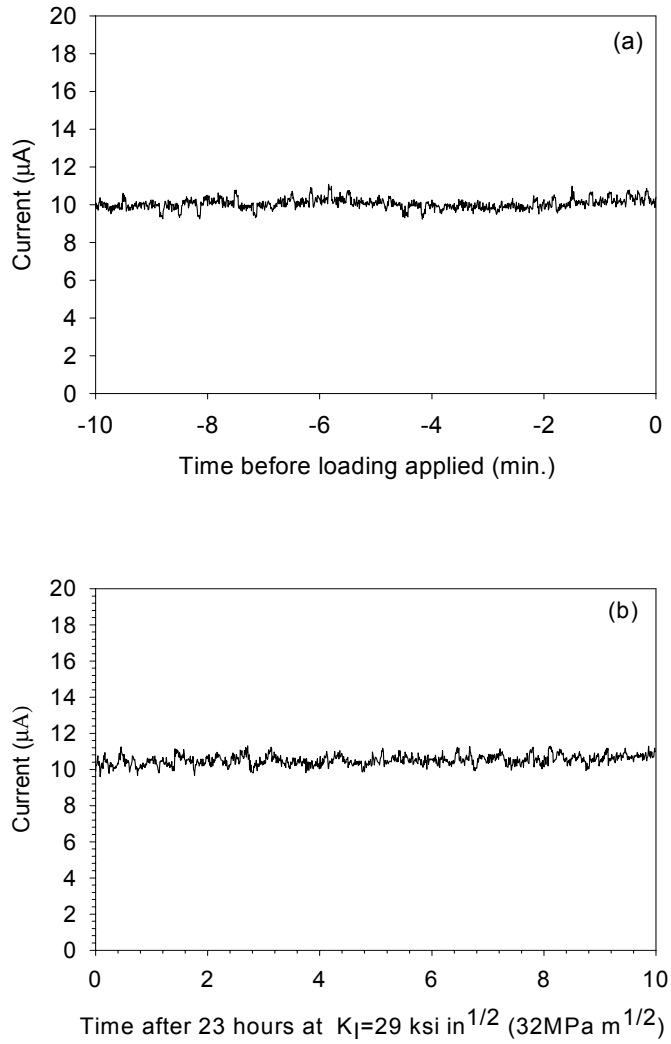

Figure 1.13. The (electron) coupling current vs. time before load application (a) and after 23 hours at $K_I = 32$ MPa$\sqrt{m}$ (29 ksi$\sqrt{in}$); (b) in 5 M NaOH at 70 °C.

1.5: DISCUSSION

Previous work [2] on the intergranular stress corrosion cracking of Type 304 SS in high temperature aqueous systems showed that the pulses in the coupling current were of a single frequency (or at least of a very narrow band in frequency) and that the fluctuations occurred in "packets" of four to thirteen fluctuations separated by brief periods of high frequency noise. The uniformity of the fluctuations within each packet was evidenced by the fact that it was not necessary to Fourier transform the time domain data in order to reveal the periodic nature of the noise. The noise signature indicates that the crack advances by one brittle micro fracture event at a time [2], probably occurring on a less-than-favorably oriented grain face with respect to the principal stress vector. Once the crack traverses the grain face and intersects a favorably

oriented face (note that the crack propagates intergranularly), the crack advances rapidly, resulting in the burst of high frequency, low amplitude noise.

For AISI 4340 steel in NaOH solution at 70 ºC, the results show that the susceptibility to caustic SCC increases with NaOH concentration. No crack propagation is observed in 1 M and 5 M NaOH solutions, and the noise in the (electron) coupling current comprises low amplitude, random fluctuations that are characteristic of general corrosion. Individual brittle micro fracture events are observed at low crack growth rate in 6 M NaOH solution. In more concentrated NaOH solution (8 M and 12 M), on the other hand, the noise in the (electron) coupling current displays periodic features that are best observed by Fourier transformation. It is postulated that caustic cracking in this high strength steel in the more concentrated caustic environments advances by many micro cracks occurring simultaneously. A transient in the coupling current signals each micro crack advance and, since many events occur at any given time, the coupling current appears as semi random fluctuations on a high mean.

Hydrogen embrittlement has been postulated to be the mechanism for environment-assisted cracking in high strength steels in caustic environments[7]. Substantial evidence exists in the literature that the chemical environment at the tip of a stress corrosion crack can differ markedly from the bulk solution composition, due to the "occluded cell" (differential aeration) effect. Brown et al.[8, 9] found that the solution at the tip of a crack in AISI 4340 steel in chloride containing solution always had a pH of 3.5 to 3.9, even though the bulk pH varied between 2 and 10. The establishment, in that case, of a steady state pH at the tip is due to hydrolysis equilibria involving the soluble corrosion products (e.g., Fe^{2+}).

The potential at the crack tip for high-strength steel always lies at or below the “hydrogen line” for the prevailing crack tip pH, for a variety of external conditions. Thus, the observations of this work can be explained by a brittle micro fracture mechanism, in which the events are possibly induced by hydrogen. We postulate that the large current exiting the crack mouth, which has been detected by the ZRA measurements reported here, generates a lower pH at the crack tip and that hydrogen is injected into the local metal matrix ahead of the crack tip. Hydrogen atoms then diffuse to the grain boundaries where embrittlement occurs by pressurization of micro voids or by chemical decohesion via reaction with segregated metalloids (e.g., P, Si, N)[10]. In any event, the periodic fracture events are initiated at points ahead of the crack at which the hydrostatic stress and the hydrogen concentration exceed critical conditions. This mechanism is proposed, in spite of the fact that the environment external to the crack is highly alkaline and oxidizing. Furthermore, we note that the fractographic characteristics of caustic cracking in AISI 4340 steel in NaOH solution, as observed in this work, are very similar as those found for hydrogen embrittlement in precracked specimens of the same steel in gaseous hydrogen[11], an environment in which anodic dissolution is not possible.

Finally, assuming that the fracture events are semi-circular in geometry of radius r and that the frequency at which they occur is f, the crack growth rate can be written as[2]

$$\frac{dL}{dt} = \frac{2r^2 f}{B_n} \tag{1}$$

where B_n is the specimen thickness at the groove. Equation (1) is readily rearranged to yield the micro fracture dimension as

$$r = \sqrt{\frac{B_n . dL/dt}{2f}} \tag{2}$$

For the 6 M NaOH case, dL/dt = 5.3 x 10^{-8} cm/s, B_n = 2.7 cm, and $f \approx 0.003$ s^{-1} (Figure 1.11), yielding a micro fracture dimension of ≈ 49 μm. Note that the fracture frequency is somewhat subjective, because it depends upon what is counted as a "fracture event". In the present case, eleven events were counted over the sixty minutes recorded in Figure 1.11, resulting in the value given above for *f*. The calculated fracture dimension may be compared with the 3 μm dimension found for the fracture of sensitized Type 304 SS in high temperature water[2]. It is likely, however, that larger micro fracture events give rise to the more intense current transients, so that the 49 μm dimension estimated above probably represents the upper end of a distribution in this quantity. Because the dimension of a slip event should be a small multiple of the Burger's vector (nanometers), the fracture dimension appears to be much too large to be consistent with the slip/dissolution/repassivation mechanism for crack advance. On the other hand, the dimension is consistent with a hydrogen embrittlement mechanism, noting that the fracture dimension is expected to correspond with the spacing of some metallurgical asperity (e.g., precipitates) on the grain boundary or with the grain size itself (note that the grain size as revealed on the fracture surface is 10 – 40 μm, Figure 1.7).

1.6: SUMMARY

The data reported here demonstrate that positive current flows through the solution from the crack to an external cathode during environmentally assisted fracture of AISI 4340 steel in concentrated (6~12 M) sodium hydroxide solution at 70 °C. The (electron) coupling current contains noise, with the amplitude of the noise and the mean current increasing with crack growth rate. Individual transients in the noise are characterized by a sudden change in the current to more negative values followed by slow recovery. The seemingly random pulses in the coupling current occurring during fracture in concentrated NaOH solution (8 M and 12 M) are attributed to the overlap of many micro cracks propagating simultaneously along the grain boundaries. At a lower NaOH concentration (6 M), individual transients become resolved in the time domain, which demonstrates that the crack advances by individually resolved, micro fracture events of about 49 μm in dimension. The discrete events are postulated to be hydrogen induced, and the mechanism of caustic cracking of AISI 4340 steel is considered to be hydrogen embrittlement along grain boundaries. At a still lower NaOH concentrations of 1 M and 5 M, no transients were observed in the coupling current, nor was there any evidence of environment assisted crack growth. The coupling current data are consistent with a hydrogen embrittlement mechanism for crack advance.

1.7: REFERENCES

1. G. L. Edgemon, M. J. Danielson, and G. E. C. Bell, J. Nuclear Materials, **245**, 201 (1997).
2. M. P. Manahan, Sr, D. D. Macdonald and A. J. Peterson, Jr., Corros. Sci, **37**, 189 (1995).
3. D. A. Vermilyea and R. B. Diegle, Corrosion, **32**, 26 (1976).
4. J. C. Scully, Corros. Sci., **20**, 997 (1980).

5. D. D. Macdonald and M. Urquidi-Macdonald, Corros. Sci., **32**, 51 (1991).
6. A. J. Sedriks, Stress Corrosion Cracking Test Methods, an official NACE publication, 1990, p.39
7. R. C. Newman and R. P. M. Procter, British Corrosion Journal, **25**, 259 (1990).
8. B. F. Brown, ed., Stress Corrosion Cracking in High Strength Steels and in Titanium and Aluminum Alloys, Naval Research Laboratory, 1972, p.80-145
9. B. F. Brown, Stress Corrosion Cracking and Hydrogen Embrittlement of Iron Base Alloys, Unieux-Firminy, France, June 12-16, 1973, NACE International, USA, p.747-750
10. B. Craig, ASM Handbook, ASM International, vol. 13, Corrosion, 1990, p.163
11. D. Hardie and S. Liu, Corros. Sci., **38**, 721 (1996).

Chapter 2

NATURE OF THE PASSIVE FILM ON NICKEL

2.1: ABSTRACT

The passive film formed anodically on nickel in borate buffer solution in both the passive and transpassive regions is found to be p-type, corresponding to a preponderance of metal vacancies (over oxygen vacancies and nickel interstitials) in the barrier layer. However, at high anodic potentials, some n-type character was detected by Mott-Schottky analysis, which is probably due to the presence of free charge carriers (electrons) from the evolution of oxygen and or the oxidative ejection of Ni^{3+} at the barrier layer/outer layer interface. The p-type character of the film is consistent with the diagnostic criteria obtained from the Point Defect Model for a passive film, in which the majority defect in the NiO barrier layer is the metal vacancy. The transpassive state is postulated to comprise a thick, porous oxide film on the surface, with the current probably being due to the oxidative ejection of Ni^{3+} species from the barrier layer and oxygen evolution within the pores, or both.

2.2: INTRODUCTION

Nickel is used extensively in structural alloys, both as an alloy base (e.g., in nickel-base alloys, such as Alloy 600) and as an alloying element in austenitic stainless steels (for example). Commercially "pure" nickel, Alloy 200, is used extensively for the containment of caustic solutions, and while the cost is significantly higher than that of carbon steel, the superior corrosion performance of nickel over iron at high pH frequently makes Ni-200 the material of choice for caustic service. Not surprisingly, the passivity of nickel has been studied extensively. Nickel (II) oxide (NiO) is generally accepted as the main component in the passive film on nickel in both acidic and alkaline environments. Okuyama et al. [1] studied the passive films on nickel in borate buffer (pH 8.4) solution and concluded that NiO was responsible for passivity. However, their analysis was based on polarization experiments and thermodynamic calculations, which alone cannot distinguished between NiO and $Ni(OH)_2$. Finally, they concluded that Ni_2O_3 was formed along with NiO, thereby creating a mixed oxide structure. Oblonsky et al. [2] using surface enhanced Raman spectroscopy (SERS) with electrodeposited gold, found that the passive film formed on nickel in borate buffer solution upon stepping the potential from $-1V_{SCE}$ to $+0.1V_{SCE}$ consists only of amorphous $Ni(OH)_2$. This structure prevails until 0.6V. When the potential was changed from –1V to $0.9V_{SCE}$, NiOOH-like species are formed. These results do not confirm previous findings that indicate the presence of both $Ni(OH)_2$ and NiO on the nickel surface [3]; however, Raman spectroscopy has poor depth resolution, and it is doubtful whether the technique could detect a thin (1 – 3 nm) NiO barrier layer beneath a thick (> 2 nm) $Ni(OH)_2$ outer layer. While the authors favored a bilayer model, in which the $Ni(OH)_2$ layer was first formed by dissolution/precipitation, their findings are at odds with the great body of literature demonstrating the existence of an NiO barrier layer. For example, recent angle resolved XPS studies on nickel and nickel alloys clearly show the existence of an inner, NiO layer and an outer, $Ni(OH)_2$ layer [4,5]. Because XPS has much better depth resolution than SERS, and because it is capable of clearly differentiating oxygen in NiO from the same species in $Ni(OH)_2$, we posit that the XPS evidence is unequivocal for a bilayer structure comprising an inner barrier

layer of NiO and an outer layer of $Ni(OH)_2$. A bilayer structure was also found by Nishimura [6], who stated that a passive film formed on Ni in neutral and weakly alkaline solutions was composed of $Ni(OH)_2$ (outer layer) and NiO (inner layer). Sato et al. [7] studied the electrochemical behavior of Ni in borate buffer using ellipsometry and coulometry, and proposed that films formed at potentials above $0.8V_{SCE}$ consist of Ni_2O_3, which is reduced to NiO under cathodic polarization. We should note, however, that the evidence for the existence of "Ni_2O_3" as a stoichiometric compound is tenuous. (Ref 8?)

A large number of photo electrochemical studies of the semi conducting properties of Ni oxides have been reported [Ref. 9 and citations therein]. These studies show that Ni(II) oxides in both hydrated and dehydrated forms behave like p-type semiconductors, while phases containing Ni at higher oxidation states behave like n-type semiconductors. The above results are consistent with the findings by Wilhelm et al. [10], who showed that the passive film on nickel displays n-type or p-type photocurrents, depending upon the electrode potential. The authors attributed the cathodic photocurrents to p-NiO whilst n-type (anodic) photocurrents were explained in terms of further oxidation of Ni by photo-generated holes. p-type semi conductive properties of passive films on nickel result from the high concentration of cation vacancies, which act as acceptors levels [11-14]. Sunseri et al. [9] found that the passive films formed on Ni at high anodic potentials ($0.85V_{sce}$?) in borate buffer solutions showed n-type photo effects after 70 hr of polarization. While the photoelectrochemical behavior of nickel at lower potentials in the passive range has been extensively studied, as evidenced by the literature cited above, the same cannot be said for the higher potential region. Accordingly, in this study, we have explored the semi conductive properties of the passive film formed on nickel in borate buffer solution, with particular emphasis on the upper end of the passive state and the transpassive state.

2.3: EXPERIMENTAL

All electrochemical studies were carried out in a three-electrode PTFE electrochemical cell. The counter electrode was a Pt wire, and all potentials were measured against a saturated calomel electrode (SCE) that was connected to the cell via a Luggin probe. The working electrode was a pure nickel wire (Alfa, 99.99%), which was embedded in two-component epoxy resin and mounted in a PCV holder. The end face of the electrode, of geometric area 0.008 cm^2, was abraded with 1200 grit SiC paper, polished with 0.05 μm Al_2O_3 powder and cleaned in an ultrasonic cleaner. All experiments were performed at ambient temperature (22 ± 2°C) in pH 8.4 borate buffer solution (0.075 M $Na_2B_4O_7 \bullet 10H_2O$+ 0.3 M H_3BO_3). The solution was de aerated with "zero-grade" N_2. Prior to all experiments, the nickel electrode was cathodically polarized at –1.0 V_{sce} for 2 min to remove the air formed film. The potential was stepped to different film formation values, ranging from 0.3 V_{SCE} to1.2 V_{sce}.

Electrochemical experiments were performed using a Solartron 1286 Electrochemical Interface. The electrochemical impedance data were recorded with a Solartron 1250 Frequency Response Analyzer (FRA), using an excitation voltage of 10 mV (peak-to-peak) and an applied frequency ranging from 65 kHz to 1 mHz. The capacitance of the interface was measured at constant frequency of 1 kHz.

2.4: RESULTS AND DISCUSSION

The anodic polarization curve recorded under potentiodynamic conditions (Figure 2.1) shows an anodic active peak at –0.75 V_{sce} followed by a transition to passivity. The transpassive region begins at $+0.4V_{sce}$, as indicated by a steep rise in the current density. The measured

polarization curve is consistent with those observed under similar conditions by other authors. Note that the passive current density appears to be independent of voltage at potentials ranging from *ca*. –0.5 V_{sce} to 0.3 V_{sce}. Previous work by Macdonald, Biaggio, and Song [13] has shown that the logarithm of the steady state current density is, in fact, an increasing, linear function of voltage in this region, and that this relationship is diagnostic of the principal defect in the barrier layer being the cation vacancy.

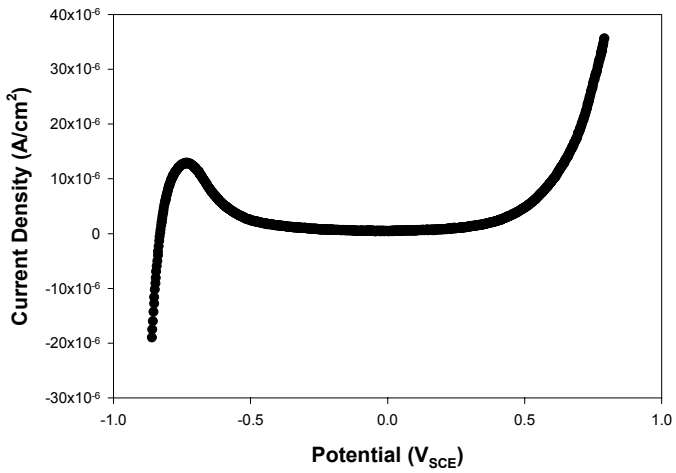

Figure 2.1. Potentiodynamic polarization curve for nickel in borate buffer solution (pH = 8.4) at 22 ^{o}C. Voltage sweep rate = 1 mV/s.

The steady-state current density (i_{ss}) for passive nickel in borate buffer solution was measured as a function of formation potential at voltages ranging from 0.3 V_{sce} to 1.1 V_{sce}, a range that extends into the transpassive region (Figure 2.2). At the lower end of this range (Region I), a linear dependence of $ln(i_{ss})$ on the applied potential is observed, with the passive current density increasing with increasing formation potential, in agreement with previous findings [13]. However, at higher potentials (> 0.7 V_{sce}), a second linear $ln(i_{ss})$ vs. voltage relationship is observed (Region II), which has a slope that is considerably greater than that in Region I (20.93 V^{-1} versus 3.21 V^{-1}, respectively). While it is tempting to attribute this second region to processes that occur within the passive film, we should note that the potential range lies within the transpassive region where oxygen evolution also occurs. Thus, any interpretation of the current density/voltage behavior in this region is complicated by the flow of charge carriers through the film from the metal to the film/solution interface, where water is oxidized to molecular oxygen.

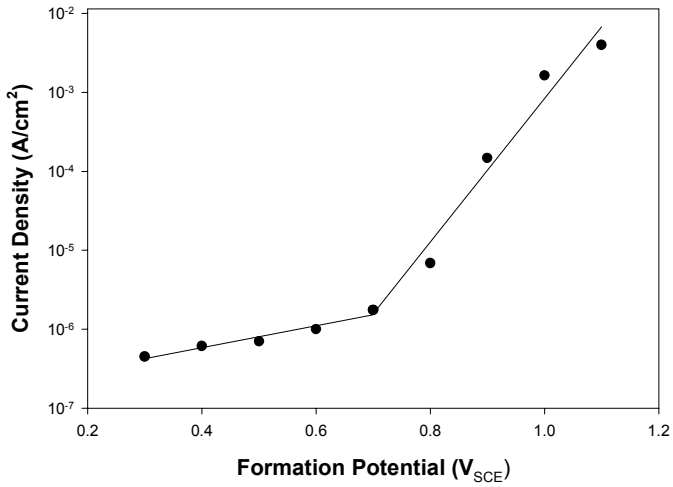

Figure 2.2. Dependence of the steady state passive current density for nickel in borate buffer solution (pH = 8.4) at 22 ^{o}C on the passive film formation potential.

Over the past 20 years, we have developed the Point Defect Model (PDM) [Refs 14-16, and citations therein] for the passive state that provides an atomistic description of the growth and breakdown of passive films under steady state and transient conditions. The PDM, which predicts the existence of steady states in the passive current and film thickness, accounts for the linear dependencies of the steady-state film thickness and logarithm of the passive steady state current density on applied potential. This theory assumes that the potential applied across the metal/film/solution interphase occurs as a potential drop across the film, as well as drops in voltage across the metal/film and film/solution interfaces. The linear dependence of film thickness on applied voltage implies that the electric field strength within the film is independent of voltage, even when the applied potential is changed over a wide range. Additionally, the PDM yields a number of diagnostic criteria that can be used to determine the identity of the principal crystallographic and electronic defects, provided that the film is a defect semiconductor (Table 2.1 in Ref. 13]. Bulk NiO is a p-type semiconductor with its conductivity being attributed to cation deficiency. The PDM predicts that the logarithm of the steady-state current density for this type of conduction mechanism should increase linearly with applied potential, as observed, indicating that the barrier oxide layer on nickel in the passive region (Region I) is also a p-type semi conductor.

Thus, the PDM predicts that the steady state current density for a cation vacancy conducting barrier layer has the following functional form

$$i_{ss} = \delta F k_4^0 e^{\alpha_4 \alpha \delta \gamma V} \tag{1}$$

where δ is the oxidation state of the nickel species being ejected from the barrier layer ($\delta = 2$ for the passive state), k^0_4 and α_4 are the standard rate constant and the transfer coefficient, respectively, for the cation ejection reaction at the barrier layer/outer layer interface ($Ni_{Ni} \rightarrow Ni^{2+} + V_{Ni}^{2'}$), α is the polarizability of the barrier layer/outer layer interface, and $\gamma = F/RT$. Thus, a plot of $ln(i_{ss})$ versus V should be linear with a slope of $\alpha_4 \alpha \delta \gamma$ and an intercept at 0.0 V_{she} of

$ln(\delta F k^0_4)$. Noting that $\gamma = 39.32\ V^{-1}$, $\alpha = 0.22$ [16], and $\delta = 2$, we obtain $k^0_4 = 3.1 \times 10^{-13}$ mol/cm^2.s and $\alpha_4 = 0.19$. The small value for α_4 indicates that charge separation is not highly developed in the transition state for the cation ejection reaction at the barrier layer/outer layer interface; that is, the transition state occurs at only a small displacement of the cation from its normal site within a cation vacancy in the barrier layer surface.

The thickness of the passive film on nickel formed in borate buffer solution was measured ellipsometrically and coulometrically by Sato et al. [7]. The results indicate a linear relationship between the film thickness and the formation voltage for the passive film formed in the primary passive region, in agreement with the predictions of the Point Defect Model [xx]. The passive films on nickel formed in borate buffer solution at high anodic potentials were very thick, and the thickness did not depend on formation voltage. The lack of a dependence of the film thickness on the voltage in the transpassive state may well reflect that the passive film is dominated by the porous, outer layer that forms by the oxidative ejection of Ni^{2+} from the barrier layer to form Ni^{3+} or even Ni^{4+}, followed by hydrolysis to produce porous NiOOH or even "NiO_2". The formation of a porous film on the metal is consistent with the impedance data discussed below. Recent theoretical work using the PDM [xx] shows that if transpassive dissolution can be attributed to the oxidative ejection of a cation from the barrier layer (i.e., $Ni_{Ni} \rightarrow Ni^{3+} + V_{Ni}^{2/} + e^-$) and/or oxidative dissolution of the barrier layer itself ($NiO + 2H^+ \rightarrow Ni^{3+} + H_2O + e^-$), then the barrier layer is greatly reduced in thickness or even disappears. Consequently, a grater fraction of the applied potential appears across the metal/film or metal solution interface, resulting in a greatly enhanced current. However, it may also be that the current observed in the second (high potential region (Region II, Figure 2.9) is not due to film growth or metal dissolution processes at all but, instead, reflects a charge transfer process involving the solvent. Oxygen evolution is such a process, which is expected to obey Tafel's equation resulting in the observed linear dependence of the logarithm of the current density on applied voltage.

Impedance measurements

Impedance measurements on passive nickel in borate buffer solution were performed as a function of formation potential. Figure 2.3 shows a typical Nyquist plot for passive nickel at potentials ranging from $0.3V_{SCE}$ to $0.6V_{SCE}$; that is, within Region I. In the high frequency range the complex plot is nearly a vertical straight line with the slope being independent of formation voltage, corresponding in the first approximation to a capacitance in series with a resistance. The results are in agreement with the findings reported by Macdonald and Smedley [xx], Madou et al. [17] and Barral et al. [18] on passive films formed on nickel in alkaline solutions, and are also in agreement with the findings of Chao, et.al. [16] for nickel in phosphate buffer solutions. These latter workers and Macdonald and Smedley [xx] showed that the Point Defect Model, corresponding to the transport of defects across the passive film, predicts the form of the impedance shown in Figure 2.3. Because defect transport is primarily due to migration under the influence of the electric field, and because the field strength is postulated (in the PDM) to be independent of the applied voltage, the impedance should also be insensitive to the film formation potential, as observed. These data therefore provide strong circumstantial evidence for the constant electric field strength postulate of the PDM.

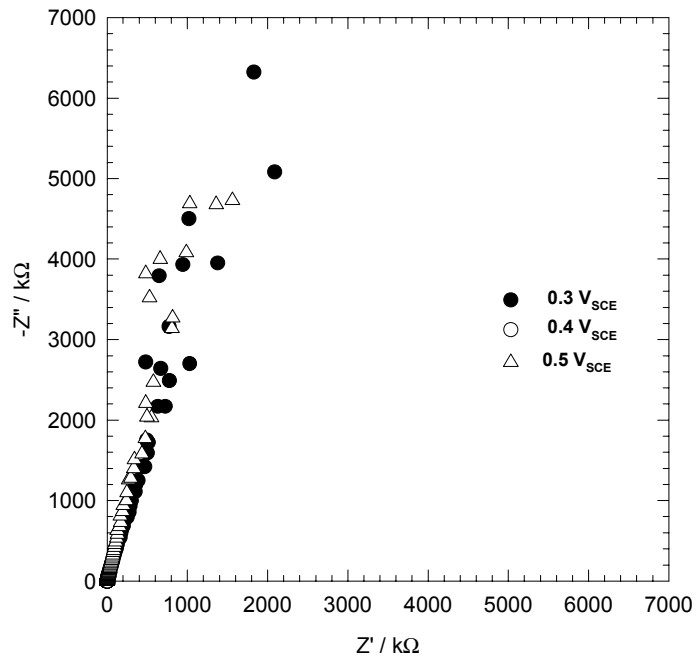

Figure 2.3. Impedance spectra for passive nickel in borate buffer solution (pH = 8.4) as a function of potential in Region I.

The impedance spectra for passive films formed on nickel in Region II are quite different from those observed in Region I. Nyquist plots for films formed at potentials ranging from $0.8V_{SCE}$ to $1.1V_{SCE}$ (Region II) are presented in Figure 2.4. Thus, for a given frequency, the specific impedance in Region II is up to a thousand times smaller than that in Region I. Assuming that the high impedance in Region I is due to the barrier layer of the passive film, the greatly reduced specific impedance in Region II is consistent with the destruction of the barrier layer. By expanding the high frequency regions of the Nyquist plots for Region II, it is found that the impedance loci comprise a high frequency semi-circle and a lower frequency diffusional response with a slope of about $\pi/8$ (Figure 2.5). Furthermore, unlike the behavior in Region I, the impedance is highly potential dependent, such that the imaginary component becomes suppressed, as the potential is made more positive. The form of the impedance is consistent with the occurrence of a charge transfer reaction in a porous film of finite thickness. This process is probably oxygen evolution occurring within a thick porous outer layer of the type described by Sato and Kudo [5], although a contribution to the current from metal dissolution cannot be discounted, particularly in light of the fact that nickel cation hydrolysis and oxygen evolution might result in local acidification within the pores even though the bulk solution is well-bufferred.

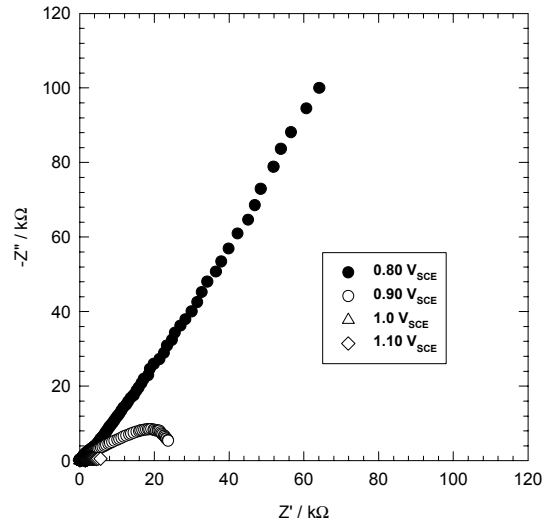

Figure 2.4. Impedance spectra for passive nickel in borate buffer solution (pH = 8.4) as a function of potential in Region II.

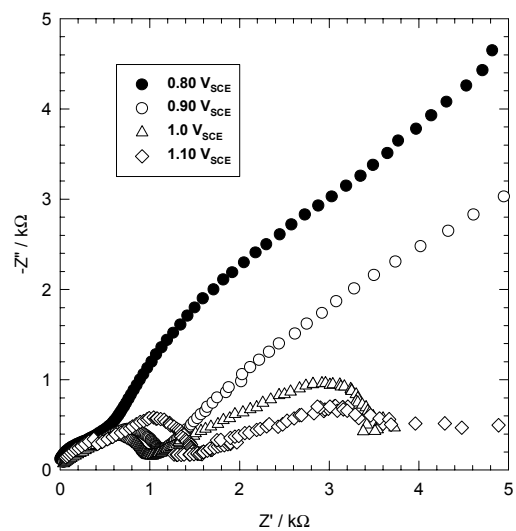

Figure 2.5. Expanded view of impedance spectra for passive nickel in borate buffer solution (pH = 8.4) as a function of potential in Region II.

Capacitance measurements

It is well known that passive films on most metals and alloys exhibit semi conductive behavior [19-25]. The most common, *in situ* method for probing the electronic properties of passive film is (besides photo electrochemistry) Mott-Schottky (M-S) analysis (capacitance measurements). In the M-S experiments reported here, the specimens were passivated for at least 24 hr at different formation potentials and the imaginary part of the impedance (*Z''*)

measured at 1 kHz was recorded as a function of the potential, as the potential was swept in the positive or negative direction at a sufficiently high rate (0.1 V/s) that the film thickness remained constant. The interfacial capacitance, C, is obtained from $C = -1/\omega Z''$. Assuming that the capacitance of the Helmholtz layer can be neglected, the measured capacitance C is equal to the "space charge" capacitance, C_{sc}. According to Mott-Schottky theory [24,26], the space charge capacitance of a p-type semiconductor is given by Equation (2),

$$\frac{1}{C^2} = \frac{-2}{\hat{\varepsilon}\varepsilon_o e N_A A^2}\left(V - V_{fb} - \frac{kT}{e}\right) \tag{2}$$

where A is the area, ε_o is the vacuum permittivity, $\hat{\varepsilon}$ is the dielectric constant of the oxide, N_A is the acceptor concentration in the passive film, V is the applied potential, V_{fb} is the flat band potential, e is the charge of the electron (1.60 x 10^{-19} C), and kT/e is about 25 mV at ambient temperature. Thus, for a p-type semi conductor, C^{-2} vs. V should be linear with a negative slope that is inversely proportional to the acceptor concentration. On the other hand, an n-type semi conductor yields a positive slope with the slope being inversely proportional to the donor concentration. C^{-2} vs. V profiles recorded for passive films formed on nickel in borate buffer at potentials within Region I (0.3-0.6 V_{SCE}) are presented in Figure 2.6. The profiles are characteristic of p-type semiconductors, displaying a narrow linear region between 0.0 V_{SCE} and –0.2 V_{SCE}. The shortness of the voltage range over which the depletion region governs the impedance behavior, presumably is due to the high doping level of the oxide.

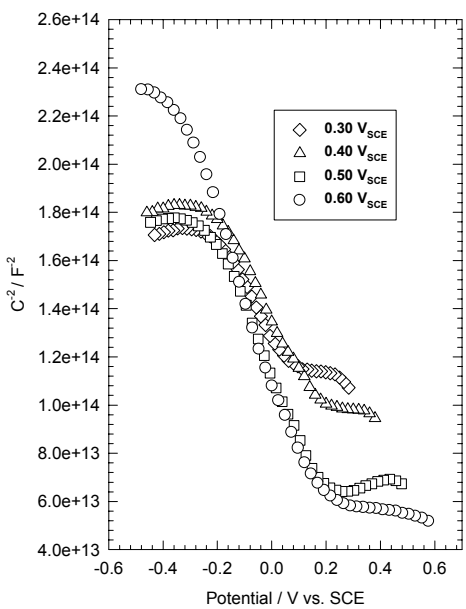

Figure 2.6. Mott-Schottky plots for passive nickel in borate buffer solution (pH = 8.4) as a function of potential in Region I.

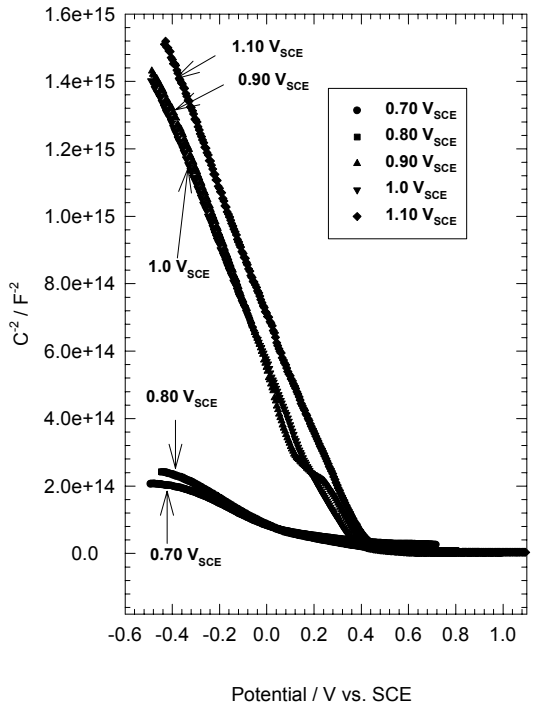

Figure 2.7. Mott-Schottky plots for passive nickel in borate buffer solution (pH = 8.4) as a function of potential in Region II.

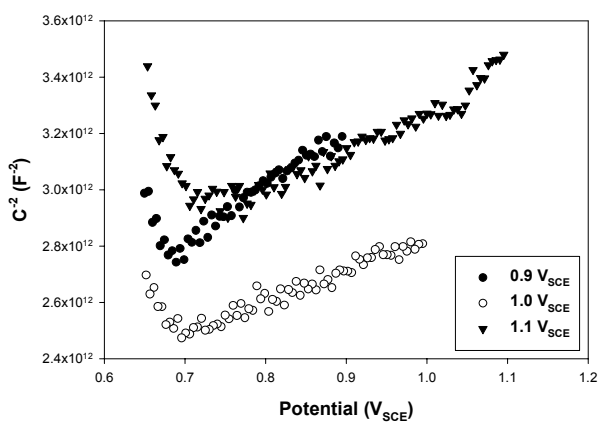

Figure 2.8. Expanded Mott-Schottky plots for passive nickel in borate buffer solution (pH = 8.4) as a function of potential in Region II for applied voltages of 0.90 V_{SCE}, 1.00 V_{SCE}, and 1.10V_{SCE}.

The C^{-2} vs. V profiles for films formed at high anodic potentials (Region II) are presented in Figure 2.7. Again, the profiles are characteristic of p-type semiconductors. However, by expanding the profiles at their initial part we definitely observe profiles that are

characteristic of n-type behavior (Figure 2.8). The flat band potentials estimated from Figures 2.7 and 2.8 agree well the literature data [25] for highly doped materials. The calculated flat band potential (V_{fb}) for the passive film on nickel in Region I was found to vary with formation voltage in a manner that is observed for n-type passive films formed on iron [26] and tungsten [27] (V_{fb} decreases with increasing film formation voltage). However, for the passive films formed in the transpassive region (Region II), if it exists, V_{fb} does not depend on formation voltage.

2.5: SUMMARY AND CONCLUSIONS

The passive film formed anodically on nickel in borate buffer solution in both the passive and transpassive regions is found to be p-type, corresponding to a preponderance of metal vacancies (over oxygen vacancies and nickel interstitials) in the barrier layer. However, at high anodic potentials, some n-type character was detected by Mott-Schottky analysis, which is probably due to the presence of free charge carriers (electrons) from the evolution of oxygen at the barrier layer/outer layer interface. The p-type character of the film is consistent with the diagnostic criteria obtained from the Point Defect Model for a passive film, in which the majority defect is the metal vacancy. At transpassive potentials, the impedance data are consistent with the formation of a thick, porous anodic oxide or oxyhydroxide film on the metal surface with charge transfer being due to the oxidative ejection of Ni(III) or Ni(IV) species from the barrier layer or oxygen evolution within the pores, or both.

2.6: REFERENCES

1. M.Okuyama and S. Haruyama, *Corr. Sci*. 14, 1 (1974).
2. L.J. Oblonsky and T.M. Devine, *J. Electrochem. Soc*., 142, 3677 (1995).
3. C.A. Melendres and M. Pankuch, *J. Electroanal. Chem*., 333, 203 (1992).
4. L. Zhang, and D. D. Macdonald, *Electrochim. Acta*, 43, 2661 (1998).
5. L. Zhang, and D. D. Macdonald, *Electrochim. Acta*, 43, 2673 (1998).
6. R. Nishimura, *Corrosion*, 43, 486 (1987).
7. N. Sato and K. Kudo, *Electrochim. Acta*, 19, 461 (1974).
8. G. Dagan, W-M Shen, and M. Tomkiewicz, *J. Electrochem. Soc*., 139, 1855 (1992).
9. C. Sunseri, S. Piazza, and F.Di Quarto, *Materials Science Forum*, v.185-188, 435 (1995).
10. S.M Wilhelm and N. Hackerman, *J. Electrochem. Soc*., 128, 1668 (1981).
11. D.D. Macdonald and S.I Smedly, *Electrochim. Acta*, 35, 1949 (1990)
12. D.D. Macdonald and M. Urquidi-Macdonald, *J. Electrochem. Soc*., 137, 2395 (1990).
13. D.D. Macdonald, S.R. Biaggio and H. Song, *J. Electrochem. Soc*., 139, 170 (1992).
14. D.D. Macdonald, *Pure Appl. Chem*., 71, 951 (1999).
15. D.D. Macdonald, K.M. Ismail, and E. Sikora, *J. Electrochem. Soc*., 146, 3141 (1998).
16. M.J. Madou and M.C.H. McKubre, *J. Electrochem. Soc*., 130, 1056 (1983).

17. G. Barral, F. Njanjo-Eyoke, S. Maximovitch, *Electrochim. Acta*, 40, 2815 (1995).

18. C.Y. Chao, L.F. Lin and D.D.Macdonald, *J. Electrochem. Soc*., 129, 1874 (1982).

19. U. Stimming and J.W. Schultze, *Ber. Bunsenges. Phys. Chem*., 80, 1297 (1976).

20. U. Stimming, *Electrochim. Acta*, 31, 415 (1986).

21. P. Schmuki and H. Bohni, *J. Electrochem. Soc*., 139, 1908 (1992).

22. E. Sikora and D.D. Macdonald, *Solid State Ionics*, 94, 141 (1997).

23. P.C. Searson, R.M. Latanison and U. Stimming, *J. Electrochem. Soc*., 135, 1358 (1988).

24. S.R. Morrison, Electrochemistry at Semiconductor and Oxidized Metal Electrodes, (1980).

25. J. Sikora, E. Sikora, and D.D. Macdonald, *Electrochim. Acta*, 1999 (in press).

26. D.M. Tench and E. Yeager, *J. Electrochem. Soc*., 120, 164 (1973).

27. E.Sikora and D.D. Macdonald, J. Electrochem. Soc., submitted (2000).

28. E. Sikora, J. Sikora, and D.D. Macdonald, *Electrochim. Acta*, 41, 783, 1996.

CHAPTER 3

NEW RATE LAWS FOR THE GROWTH AND REDUCTION OF PASSIVE FILMS

3.1: ABSTRACT

A new rate law for the growth of anodic passive films on metal surfaces is derived from the Point Defect Model (PDM). The model recognizes both the growth of the barrier oxide layer into the metal via the generation of oxygen vacancies at the metal/film interface and the dissolution of the barrier layer at the film/solution interface. The new rate law accounts for the existence of a steady state in film thickness, as well as for the transients in thickness and film growth current as the potential is stepped in the positive or negative direction from an initial steady state. The predictions of the PDM, with respect to the thickness of the barrier layer, are compared with those of the High Field Model. It is shown that the latter cannot account for the existence of steady states or the decrease in barrier layer thickness on stepping the potential in the negative direction. The predicted transients in film thickness and growth current density are found to be in good fidelity with the measured transients on tungsten in pH = 1.5 phosphate buffer solution as the voltage is cycled between 10 V_{sce} and 6 V_{sce}. Finally, the new rate law accounts for passive film thinning under negative potential step conditions as the pH is changed over the range of 1.5 to 5.1 and as the initial and final voltages are changed in a systematic manner, such that the voltage excursion is constant.

3.2: INTRODUCTION

Recently [1], it was demonstrated that the potentiostatic current transients for the growth of passive films on zirconium, titanium, tungsten, and tantalum are inconsistent with the predictions of the high field model (HFM) [2-4]. Thus, the HFM postulates that the electric field strength within the film decreases with the inverse of the film thickness as the film thickens. On the other hand, the current transient data were found to be consistent with the postulate that the electric field strength is insensitive to changes in film thickness, which is the basis of the Point Defect Model (PDM) [5]. The insensitivity of the field strength to thickness is explained by the occurrence of band-to-band tunneling ("Esaki tunneling") of charge carriers (electrons and holes) within the film, such that the field strength becomes buffered against any process that tends to increase its value [5]. Thus, because the internal tunneling current is exponentially dependent on the field, any increase in the potential gradient will cause a massive separation of charge, which will generate a counter field that will effectively buffer the potential distribution and hence maintain the field constant. Discrimination between the two models (HFM and the PDM) was made on the basis of the diagnostic relationship $\sqrt{-i'/i_{ss}(i-i_{ss})} = \sigma \ln(i)$, where i' is the differential di/dt, i is the current density, and i_{ss} is the steady state current density (i.e., the current density for $t \to \infty$). The HFM predicts, that for films that are formed primarily by the movement of oxygen vacancies (which is the case for the "valve" metals), the quantity σ should be greater than 0, whereas the PDM predicts that $\sigma = 0$. The latter relationship was found for the metals employed in the previous study [1].

The purpose of this paper is to present theoretical and experimental analyses of transients in film thickness and film growth current density on tungsten in phosphate buffer solution. We show that the transients in thickness and current also contain diagnostic information, in that the HFM, at least in its original form [2-5], does not predict a decrease in film thickness (only a decrease in the rate of thickening) nor does it predict the form of the current transient when the voltage is stepped in the negative direction from an initial non steady state. On the other hand, the PDM predicts that the film thickness, and not just the rate of thickening, decreases due to the rate of dissolution at the film/solution interface exceeding the rate of film growth of the barrier oxide layer into the metal at the metal/film interface. Furthermore, the HFM does not recognize the existence of simultaneous steady states in the film thickness and the current, an issue that has been addressed earlier [6]. These highly diagnostic relationships are illustrated by reference to experimental data for tungsten in phosphoric acid that were previously reported [6].

Metal | **Barrier Oxide Layer** | **Solution**

(1) $m + V_M^{\chi'} = M_M + v_m + \chi e'$

(2) $m = M_i^{\chi+} + v_m + \chi e^-$

(3) $m = M_M + \frac{\chi}{2} V_{\ddot{O}} + \chi e^-$

(4) $M_M = M^{\delta+} + V_M^{\chi'} + (\delta - \chi)e^-$

(5) $M_i^{\chi+} = M^{\delta+} + (\delta - \chi)e^-$

(6) $V_{\ddot{O}} + H_2O = O_O + 2H^+$

(7) $MO_{\chi/2} + \chi H^+ = M^{\delta+} + \frac{\chi}{2} H_2O + (\delta - \chi)e^-$

Figure 3.1. Interfacial defect generation/annihilation reactions that occur in the growth of anodic barrier oxide films according to the Point Defect Model [1]. $m =$ metal atom, $V_M^{\chi'} =$ cation vacancy on the metal sub lattice of the barrier layer, $M_i^{\chi+} =$ interstitial cation, $M_M =$ metal cation on the metal sub lattice of the barrier layer, $V_{\ddot{O}} =$ oxygen vacancy on the oxygen sub lattice of the barrier layer, $O_O =$ oxygen anion on the oxygen sub lattice of the barrier layer, $M^{\delta+} =$ metal cation in solution.

3.3: THEORY

According to the PDM [Ref. 5 and citations therein], the rate of change in the thickness of the barrier layer in a passive film can be written in the form

$$\frac{dL}{dt} = a.e^{-bL} - c \tag{1}$$

where $a = \Omega k_3^0 e^{\alpha_3(1-\alpha)\chi\gamma V} e^{-\alpha_3\chi\beta\gamma pH}$, $b = \alpha_3\chi\varepsilon\gamma$, $c = \Omega k_7 (C_{H^+} / C_{H^+}^0)^n$, ε is the electric field strength, C_{H^+} is the concentration of hydrogen ion at the film/solution interface, $C_{H^+}^0$ is the standard state concentration, such that k_7 (the rate constant for the dissolution of the film, Reaction 7, Figure 3.1) has units of mol/cm^2.s, Ω is the mol volume of the film per cation, n is the kinetic order of

the dissolution reaction at the film/solution interface with respect to H^+, α is the polarizability of the film/solution interface, β is the dependence of the potential drop across the film/solution interface on the pH, V is the applied voltage, γ = F/RT, F is Faraday's constant, R is the universal gas constant, T is the Kelvin temperature, and α_3 and k_3^0 (mol/cm^2.s) are the transfer coefficient and the standard rate constant, respectively, for the generation of oxygen vacancies at the metal/film interface (Reaction 3, Figure 3.1).

For steady state conditions, $dL/dt = 0$, so that

$$L_{ss} = (1/b)\ln(a/c) \tag{2}$$

where L_{ss} is the steady state thickness of the film. Upon substitution of the constants defined above, it is a straightforward matter to show that Equation (2) is identical to the expression that was previously derived for the steady state thickness of the film (barrier layer) [5], namely:

$$L_{ss} = \frac{1}{\varepsilon}\left[1-\alpha-\frac{\alpha\alpha_7}{\alpha_3}\left(\frac{\delta}{\chi}-1\right)\right]V + \frac{1}{\varepsilon}\left\{\frac{2.303n}{\alpha_3\chi\gamma} - \beta\left[\frac{\alpha_7}{\alpha_3}\left(\frac{\delta}{\chi}-1\right)+1\right]\right\}pH + \frac{1}{\alpha_3\chi K}\ln\left(\frac{k_3^0}{k_7^0}\right) \tag{3}$$

where K = εγ, and k_7^0 and α_7 are the standard rate constant and transfer coefficient for the film dissolution reaction, respectively. In deriving this expression, it is assumed that a change may occur in the oxidation state of a cation upon ejection from the film/solution interface or upon dissolution of the film. If no change in oxidation state occurs, which is the case for tungsten, as analyzed later in this paper, a somewhat simpler expression results in the form:

$$L_{ss} = \left(\frac{1-\alpha}{\varepsilon}\right)V + \frac{1}{\varepsilon}\left\{\frac{2.303n}{\alpha_3\chi\gamma} - \beta\right\}pH + \frac{1}{\alpha_3\chi K}\ln\left(\frac{k_3^0}{k_7^0}\right) \tag{4}$$

Note that Equations (3) and (4) predict that for a given pH the steady state film thickness varies linearly with applied voltage (Figure 3.2), which is an almost ubiquitous finding in the study of the formation of anodic passive films [5]. Furthermore, the equations predict that, for a given voltage, L_{ss} varies linearly with pH, and that for a given voltage and pH, the thickness is controlled by the ratio of the standard rate constants for the generation of oxygen vacancies at the metal/film interface [Reaction (2), Figure 3.1] and the dissolution of the film [Reaction (5)].

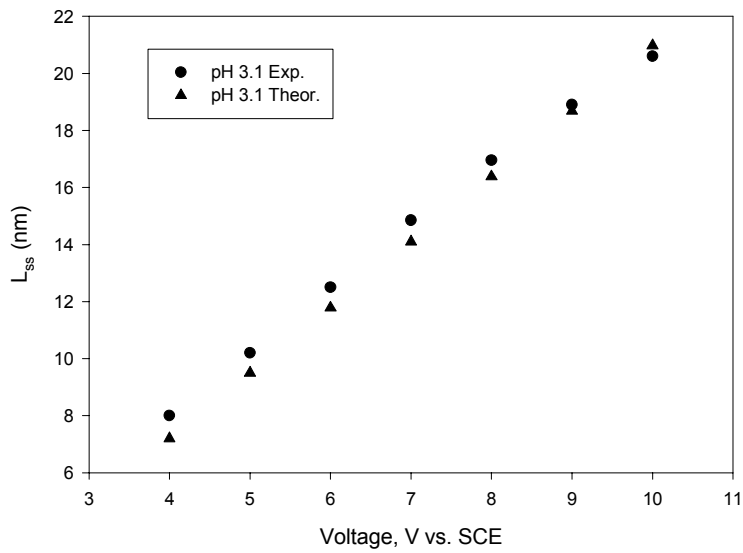

Figure 3.2. Steady state thickness versus voltage for tungsten in phosphate buffer solution as measured experimentally (capacitance, f = 1 kHz) [6] and as calculated using Equation (4) and the parameters given in Ref. 8.

Transient in Film Thickness

Equation (1) is readily integrated over the limits ($L_0, t = 0, V$) to $(L, t, V + \Delta V)$, where ΔV is the step in voltage at t = 0, to yield the transient is film thickness as

$$L(t) = L_0 + \left(\frac{1}{b}\right)\ln\left[1 + \left(\frac{a'}{c}\right)e^{-bL_0}(e^{bct} - 1)\right] - ct \tag{5}$$

where the constants and parameters are as given above. Note that. $a' = k_3^0 e^{\alpha_3(1-\alpha)\gamma(V+\Delta V)} e^{-\alpha_3\beta\gamma pH}$. It is also a straightforward matter to show that as $t \to \infty$, $L(t)$ approaches a steady state that is given by Equation (4), but with a being replaced by a'. The initial thickness, L_0, is given by Equation (4), as written. Examination of Equation (5) shows that the transient in film thickness is a combination of a linear relationship and a logarithmic function.

If the quantity bct is sufficiently small that $e^{bct} \approx 1 + bct$ and ct is much less than the second term in Equation (5), then the rate law reduces to

$$L(t) = L_0 + \left(\frac{1}{b}\right)\ln\left[1 + a'be^{-bL_0}t\right] \tag{6}$$

where the parameters are as defined above. Equation (6) has the same form as the classical logarithmic relationship [4]. Accordingly, the classical logarithmic rate law is obtained as a

special case of the more general law embodied in Equation (5). Note that for $t = 0$, the film thickness equals the initial thickness, L_0, which is the correct limiting form.

Transient in Film Growth Current

The transient in film growth current density due to the generation of oxygen vacancies at the metal/film interface and the dissolution of the film at the film/solution interface is readily calculated as

$$i = \chi F k_3 + (\delta - \chi) F k_7 (C_{H^+} / C^0_{H^+})^n \tag{7}$$

Noting that $k_3 = k_3^0 \exp(a_3 V - b_3 L - c_3 pH)$ and $k_7 = k_7^0 \exp(a_7 V + c_7 pH)$, where $a_3 = \alpha_3 (1-\alpha)\chi\gamma$, $b_3 = \alpha_3 \chi\gamma\varepsilon$, $c_3 = \alpha_3 \chi\gamma\beta$, $a_7 = \alpha_7 \alpha(\delta - \chi)\gamma$, and $c_7 = \alpha_7 \beta(\delta - \chi)\gamma$, we obtain the transient in the current as

$$i = \chi F k_3^0 e^{a_3 V} e^{-c_3 pH} X + (\delta - \chi) F k_7^0 e^{a_7 V} e^{c_7 pH} (C_{H^+} / C^0_{H^+})^n \tag{8}$$

where

$$X = \frac{c e^{-b_3 L_0}}{a' e^{-b_3 L_0} - (a' e^{-b_3 L_0} - c) e^{-bct}} \tag{9}$$

with a', b, and c being as defined in Equation (1). Note that Equation (8) applies strictly to an oxygen ion conducting film. The other two cases (cation vacancy and cation interstitial conducting films and hence the general case when all three defects are present simultaneously at significant concentrations) require the solution of a moving boundary problem ("Stefan's problem"). These cases have been solved and will be published in a separate paper. Finally, it is important to note that Equation (5) is general to all three cases, because only the generation of oxygen vacancies via Reaction (3), Figure 3.1, and their annihilation at the film/solution interface [Reaction (6)], coupled with film dissolution [Reaction (7)], lead to a change in dimension of the film.

3.4: DISCUSSION

Equations (5) and (9) represents completely new rate laws for the growth of a barrier oxide layer under potentiostatic transient conditions. These laws result from the postulate that the electric field strength is independent of the applied voltage and that the film undergoes dissolution at the barrier layer ("film")/solution interface. It is instructive to compare the PDM with the classical HFM, as developed Verwey (V) [2] and later modified by Cabrera and Mott (CM) [3]. In these models, which are still extensively used for interpreting experimental oxide film growth rate data, the electric field strength is assumed to decreases as the film thickens, and film growth is assumed to occur only at the film/solution interface, because no movement of oxygen vacancies is recognized. Furthermore, dissolution at the film/solution interface is generally not recognized and rate control is postulated to reside in cation transfer between neighboring lattice positions (V) or in cation ejection from the metal into the film (CM). These models give the film growth rate law, for potentiostatic conditions, as

$$\frac{dL}{dt} = Ae^{B/L} \tag{10}$$

where A and B can be expressed in terms of fundamental parameters (see Ref. [4]).

Equation (10) does not have an analytical solution, and the one offered by Cabrera and Mott [3] is strictly not valid (see Burstein and Davenport [7] for an excellent discussion of this issue). For our purposes, we need only note that as $t \to \infty$, $L \to \infty$, and $dL/dt \to A$. Thus, the film thickness is predicted to never reach a steady state value within finite time, which is at odds with experimental observation [6]. Furthermore, regardless of the magnitude or sign of B, the sign of dL/dt never changes, although the magnitude clearly does. Thus, regardless of whether ΔV is positive or negative, and irrespective of the magnitude of the step in voltage, the V and CM models predict that the film will continue to grow, which is again contrary to experimental observation [6]. Accordingly, the classical HFM, regardless of the form [2-4], must be rejected as being capable of describing the growth of passive films on metal surfaces.

An attempt has been made to correct the deficiencies of the HFM by introducing, in an *ad hoc* fashion, dissolution at the film/solution interface [6]. This modification removed some of the objections to the HFM, in that the model was capable of predicting a steady state in film thickness and was able to account for a change in the sign of dL/dt as the sign of ΔV changed. However, it was not able to account for the pH dependence of the steady state passive film thickness vs. applied voltage [6].

We now return to Equations (1) and (5). Equation (1) clearly predicts a steady state in film thickness, resulting in Equations (3) and (4). Furthermore, as ΔV changes sign, and hence as a changes value, but never sign, dL/dt may be positive or negative, corresponding to film growth or film thinning, respectively, depending upon the relative values of the two terms on the right side of Equation (1). Note that, because Reaction (3), Figure 3.1, is considered to be irreversible in the direction indicated, film thinning occurs exclusively via the rate of dissolution at the film/solution interface (Reaction 7, Figure 3.1) being greater than the rate of film growth at the metal/film interface (Reaction 3). This is considered to be a reasonable approximation, if the voltage is significantly more positive than the equilibrium potential for the formation of the barrier layer phase. Furthermore, Equations (3) and (4) correctly predict the linear dependencies of L_{ss} on the applied voltage (V) and pH [6]. We now show below that Equations (5) and (8) correctly account for the transients in film thickness and current, respectively.

Prior to doing this, it is first necessary to identify the rate control process in film growth, according to the PDM. Thus, as noted previously [1,5], rate control resides in the injection of charge into the film at the metal/film interface. With respect to film growth, this occurs via the generation of oxygen vacancies at the metal/film interface by Reaction 3, Figure 3.1. The charge is injected into an electric field that is *independent of the thickness of the film and the applied voltage*. Accordingly, the potential drop across the metal/film interface ($\phi_{m/f}$), which drives the oxygen vacancy formation reaction [Reaction 3, Figure 3.1], decreases linearly with increasing film thickness, namely

$$\phi_{m/f} = (1-\alpha)(V + \Delta V) - \varepsilon L - \beta.pH - \phi^0 \tag{11}$$

for $t > 0$ and $L(t) > L_{ss}$, where ϕ^0 is a constant that depends upon the selection of the potential scale. The other parameters are as previously defined. It is the formation of oxygen vacancies at the metal/film interface, in the presence of the decreasing potential drop, $\phi_{m/f}$, that constitutes

rate control in the case of the PDM. In contrast, the CM form of the HFM postulates that the rate-determining step in film growth is the injection of cations from the metal into the film in the presence of an electric field that *decreases with increasing film thickness*. The CM model gives rise to the same rate law as does the original Verwey model [2] (but with small differences in some parameters), which postulates that rate control resides in the transfer of a cation from one lattice position to another within the bulk of the film, as noted above.

Equations (5) and (8) were used to calculate the transients in film thickness and current upon stepping the applied voltage over the cycle 10 V_{sce} –> 6 V_{sce} –> 10 V_{sce} in a solution of pH = 1.5 at 25 ^{o}C (Figures 3.3 and 3.4). The parameter values employed in the simulation are as follows: k_3^0 = 1.5e-9 mol/cm^2.s, $\alpha_3 = 0.05$, k_7^0 = 1.0e-9 mol/cm^2.s, α = 0.50, β = -0.01 V, ε = 2.3e+6 V/cm, χ = δ = 6, n = 1, and Ω = 32.38 cm^3/mol cation. Few experimental data are available for the transients in thickness and current with time for passive films on metals, and those that are available have generally been derived from reflectance, capacitance, or ellipsometric measurements. We use here the transient capacitance and reflectance data of Macdonald, et. al. [6] for the growth of the anodic oxide film on tungsten in phosphoric acid solutions (Figure 3.5), in order to illustrate the points that we wish to make.

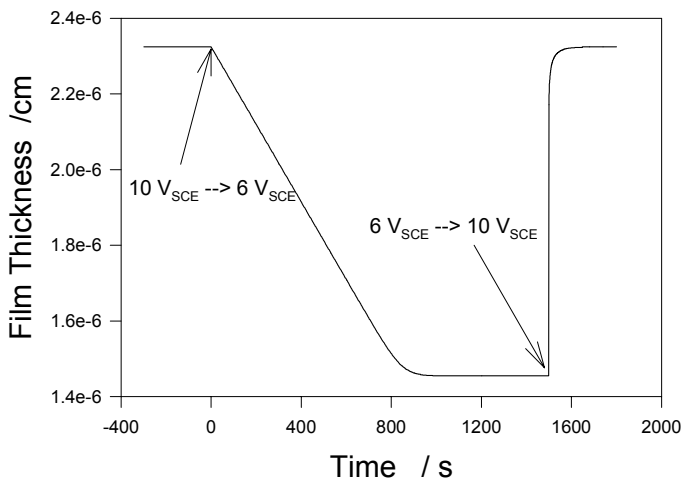

Figure 3.3. Predicted transients in passive film thickness as the voltage is stepped from 10 V_{sce} to 6 V_{sce} and then back to 10 V_{sce} at the indicated times. The parameter values used in the calculation are given in the text.

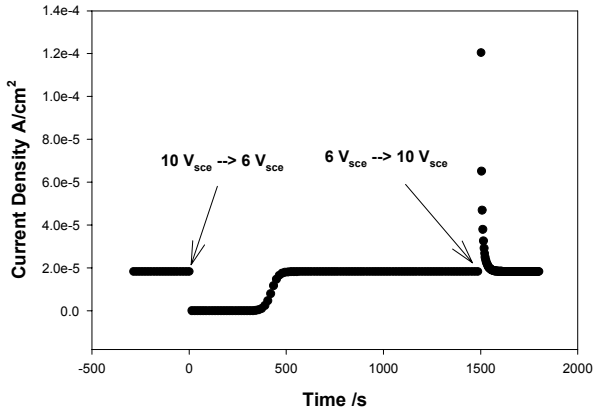

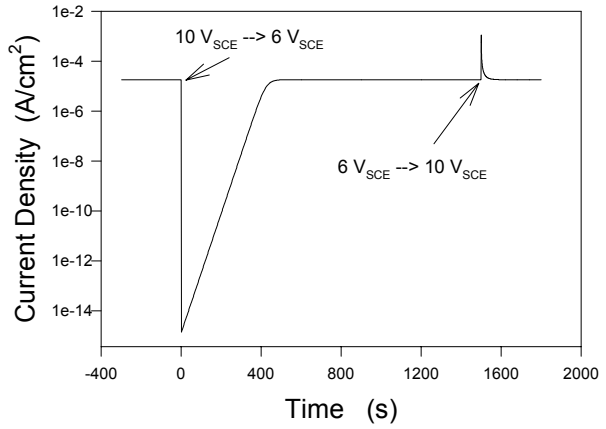

Figure 3.4. Predicted transients in passive film growth current density as the voltage is stepped from 10 V_{sce} to 6 V_{sce} and then back to 10 V_{sce} at the indicated times. The parameter values used in the calculation are given in the text. Upper plot – linear current scale, lower plot – logarithmic scale.

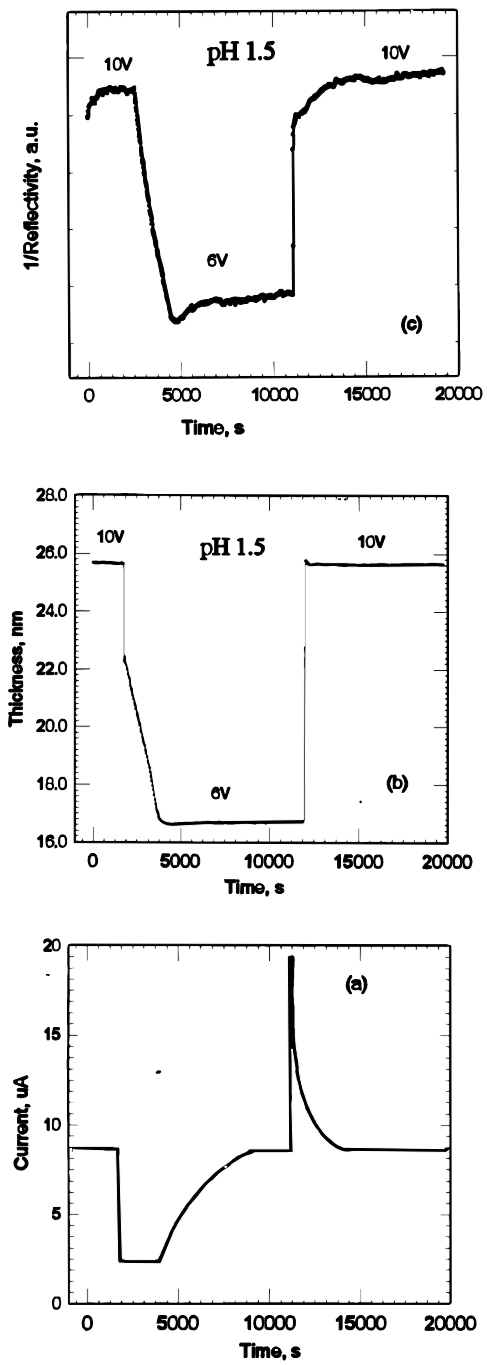

Figure 3.5. Experimental thickness and current transients for the growth and reduction of the passive film on tungsten in phosphate buffer solution (pH = 1.5) at 22 ± 2 °C upon stepping the potential over the cycle 10 V_{sce} – 6 V_{sce} –10 V_{sce}. (a) Current, (b) thickness monitored by capacitance, and (c) thickness monitored by reflectance. Data taken from Ref.(6).

Equation (5) is found to provide an excellent account of the transient, $L(t)$, as shown by a comparison between Figures 3.3 and 3.5 (b/c). Thus, Equation (5) accurately predicts the linear decrease in $L(t)$ by noting that, under these conditions, ΔV is sufficiently negative that

the first term in Equation (1) is negligible with respect to the second term, and hence that $dL/dt \approx -c$ (a constant for a given pH). Note that the sudden drop in film thickness upon stepping the potential in the negative direction, as shown in Figure 3.5(b), is an experimental artifact due to discharging of the space charge layer in the film.

Eventually, the two terms on the right side of Equation (1) become equal, principally due to the increase in the potential drop across the metal/film interface, as the film thins [see Equation (11)]. Film thinning, due to dissolution, gives rise to a continual increase in the value of the first term in Equation (1), eventually resulting in the attainment of a steady state whose thickness is described by Equation (4) with V being replaced by $V + \Delta V$ (where, in this case, ΔV is negative). At longer times, $L(t)$ remains constant in the steady state until the voltage is stepped back to 10 V_{sce}. At this point, $L(t)$ is predicted (Figure 3.3) and observed (Figures 3.5b and c) to increase sharply with time, as film growth occurs at the metal/film interface due to the production of oxygen vacancies [Reaction 3, Figure 3.1]. The increase in film thickness on stepping the voltage in the positive direction at ca. 12,000 s is not instantaneous, as shown by the calculated transient thickness vs. time in Figure 3.3. Thus, for $\Delta V > 0$, the first term on the right side of Equation (1) becomes greater than the second term and the film grows. However, as the film thickens, the voltage drop across the metal/film interface decreases, such that the rate of film growth decreases. Ultimately, the values of the two terms on the right side of Equation (1) again become equal and a new steady state is achieved. An important point to note is that the change in film thickness on cycling the applied voltage is not symmetrical, because the decrease in film thickness and the subsequent increase occur via fundamentally different processes (dissolution and oxygen vacancy generation, respectively).

Because the current and film thickness are linked by $i = (zF\rho / M)dL_+ / dt$, where z, ρ, L_+ and M are the oxidation charge number, metal density, position of the metal/film interface with respect to an external reference frame, and metal atomic weight, respectively, similar arguments can be constructed to account for the form of the transient in current. Note, however, that the calculated current transient is exponentially related to the film thickness and hence a direct comparison between the two transients is difficult to display. Nevertheless, the current transient contains all of the features observed experimentally on tungsten in phosphate buffer solution as the potential is cycled between the two voltage limits (Figures 3.4 and 3.5a). In this regard, it is important to recognize that the first plateaux in the current, which is observed immediately after stepping the potential from 10 V_{sce} to 6 V_{sce}, is an artifact of plotting the current density on a linear scale. Equation (9) actually predicts that the current increases exponentially with time [linear ln(i) vs. t] in this region until the second plateaux is reached. This is because stepping the potential from 10 V_{sce} to 6 V_{sce} results in a linear decrease in the film thickness with time and, since the film thickness appears in an exponential term in the expression for the current, an exponential increase in the current is obtained. The value of the current density at the second plateaux is the same as that for the initial state, because theory predicts that, for oxygen ion conducting films, which is the case investigated here, or for cation interstitial conducting films, the steady state current density is independent of applied voltage [5]. Finally, stepping the potential in the positive direction from the second plateaux (6 V_{sce} → 10 V_{sce}) is predicted (Figure 3.4) and found (Figure 3.5a) to result in a sharp rise in the current followed by an exponential decay. No attempt was made in this work to fit the model to the experimental data in order to extract values for the various model parameters. An analysis of this type will be published at a later date.

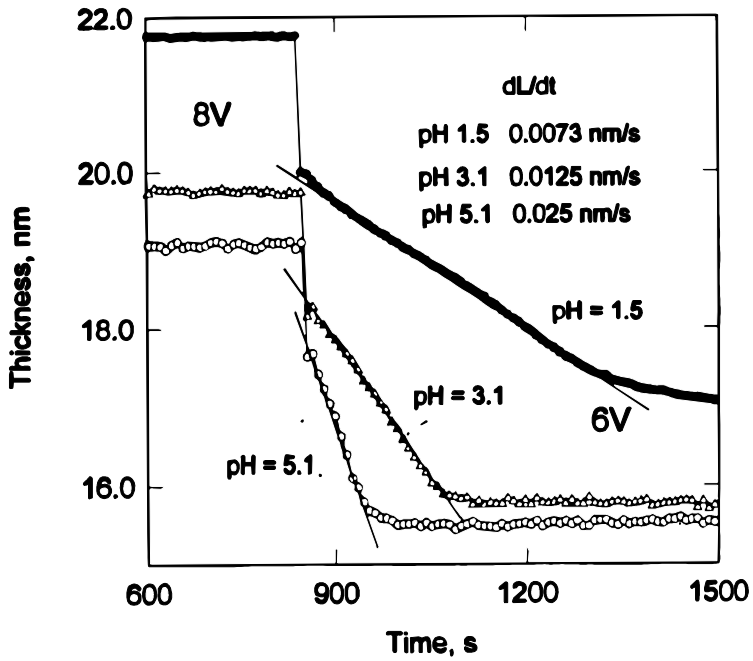

Figure 3.6. Experimental for the reduction in thickness of the passive film on tungsten in phosphate buffer solution at 22 ± 2 °C as a function of pH upon stepping the potential from 8 V_{sce} to 6 V_{sce}. Data taken from Ref. (6).

The effect of pH on the dissolution of the passive film on tungsten in phosphate buffer solution is shown in Figure 3.6. In this experiment, the sudden decrease in the applied potential from 8 V to 6 V results in the suppression of oxygen vacancy generation at the metal/film interface (i.e., of Reaction 3, Figure 3.1), with the result that the film thins at a constant rate by dissolution at the film/solution interface alone. The data show that the film thickness decreases linearly with time, in accordance with Equation (5), until the redistribution of the potential across the metal/film/solution system causes Reaction 3, Figure 3.1, to "switch on", resulting in the attainment of a new steady state at a lower film thickness, as previously noted. In terms of Equation (5), the linear relationship arises because, under these conditions (negative ΔV), a' is very small and the term within the square brackets is approximately equal to one. Thus, $L(t) \approx L_o - ct$, where c, the dissolution rate, is a function of the hydrogen ion concentration. As predicted [Equation (1)], the observed rate of film thinning is a sensitive function of pH (Figure 3.6), with values ranging from 0.025 nm/s at pH = 5.1 to 0.0073 nm/s at pH = 1.5. The inverse kinetic order with respect to $[H^+]$ is consistent with the film dissolving to form oxyanions in solution, which may be designated in general form as $WO_x(OH)_y^{6-2x-y}$, at least at the higher pH values. We note, however, that the steady state current passes through a minimum at pH = 2.5, corresponding to the isoelectric point of the oxide [5]. Accordingly, the data for the lowest pH presumably correspond to the dissolution of WO_3 to form a cationic species, possibly WO_2^{2+}.

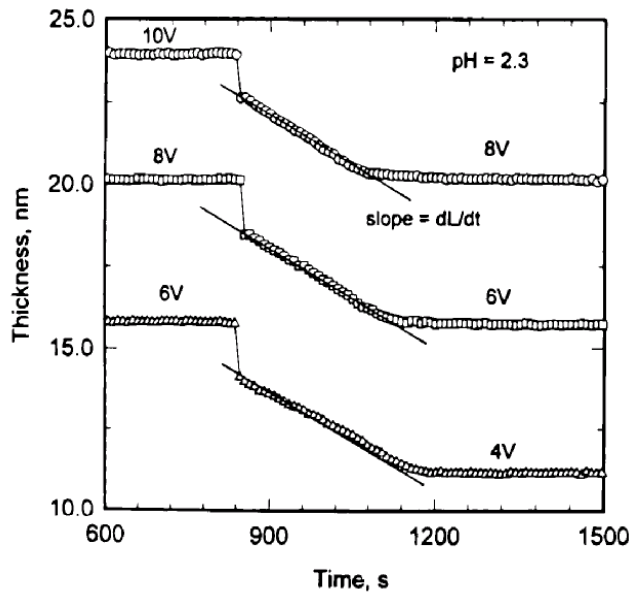

Figure 3.7. Experimental transients for the reduction in thickness of the passive film on tungsten in phosphate buffer solution at 22 ± 2 ^{o}C and pH =2.3 upon stepping the potential over different 2 V ranges. Data taken from Ref. (6).

Finally, the impact of voltage, at a given pH, on the transient in film thickness is shown in Figure 3.7. Again, in response to a negative-going potential step, the film is observed to thin linearly with time until a new steady state is established. The rate of film thinning was found to be independent of the initial and final voltages, in agreement with Equation (5), because *c* is voltage-independent by virtue of there being no change in oxidation state upon film dissolution.

3.5: SUMMARY AND CONCLUSIONS

A new rate law for the growth of a barrier oxide layer on a metal surface under anodic oxidation conditions in response to a positive- or negative-going voltage step, has been derived. The derivation assumes that the final voltage is sufficiently more positive than the equilibrium film formation potential that the generation of oxygen vacancies at the metal/film interface is irreversible. The model also assumes that oxygen vacancies are the dominant defect within the film. Because barrier layer growth involves only oxygen vacancies and film dissolution, the expressions for the transient in film thickness and for the steady state film thickness are perfectly general and are applicable regardless of the identity of the principal defect (oxygen vacancy, cation vacancy, or cation interstitial) in the film. On the other hand, the expression for the transient in current is strictly valid for oxygen vacant films. The predictions of the model with respect to the transients in thickness and current account for all of the features observed in tungsten in phosphate buffer solution.

3.6: REFERENCES

1. L. Zhang, D. D. Macdonald, E. Sikora, and J. Sikora, J. Electrochem. Soc., **145**, 898 (1998).
2. E. J. W. Verwey, Physica, **2**, 1059 (1935).

3. N. Cabrera and N. F. Mott, Rep. Prog. Phys., **12**, 163 (1948).
4. L. Young, Anodic Oxide Films, Academic Press, New York (1961).
5. D. D. Macdonald, Pure Appl. Chem., **71**, 951 (1999).
6. D. D. Macdonald, E. Sikora, and J. Sikora, Electrochim. Acta, **43**, 2851 (1998).
7. G. T. Burstein and A. J. Davenport, J. Electrochem. Soc., **136**, 936 (1989).
8. M. Al-Rifaie, "Identification of Point Defects Within Passive Films", Ph.D. Dissertation, Pennsylvania State University, 1999.

CHAPTER 4

THE PASSIVITY OF IRON IN THE PRESENCE OF EDTA
Part II. The Defect and Electronic Structures of the Barrier Layer

4.1: ABSTRACT

The passive state on iron in EDTA (Ethylene Diammine Tetraacetic Acid, disodium salt)-containing borate buffer solutions of pH = 8.4 to 10.0 at ambient temperature has been explored using potentiodynamic polarization and steady state techniques, including Mott-Schottky (MS) analysis. EDTA effectively suppresses the formation of the outer layer of the passive film thereby rendering the barrier layer amenable to direct examination. It is shown that the barrier layer on iron is a highly disordered, n-type semiconductor. The barrier layer thickness varies linearly with applied potential, whereas the steady state current density does not depend on the formation voltage. EDTA present in the solution renders the barrier layer of the passive film more defective, as indicated by MS analysis, and the donor density decreases with increasing film formation potential. These findings suggest that the dominant defects in the barrier layer are oxygen vacancies or cation interstitials, or both. No evidence of cation vacancies, which would render the barrier layer p-type and would impart a voltage dependence to the steady state current was obtained. Thus, if cation vacancies are present, they are not the dominant defect.

4.2: INTRODUCTION

The passivity of metals and alloys is the key to understanding the development of our metal-based civilization [1]. Many engineering alloys can only be used because of the existence of a thin, solid passive film that inhibits corrosion. A general consensus appears to be that the passive film on metals is a semiconductor, in which both electronic and ionic transport occurs, the exact nature of which depends upon the composition of the film from the metal-oxide interface to the oxide-solution interface. Although there is no doubt that the passive film is a semiconductor, it cannot be modeled as a classical, weakly doped semiconductor [1]. Mott-Schottky analyses of the passive films on many metals show dopant levels of 10^{20} – 10^{21} cm^{-3}, which are significantly higher than those of classical semiconductors (10^{16} – 10^{17} cm^{-3}). As noted in previous work [2], there exists a correlation of high fidelity between the crystallographic defect structure and the electrical structure (obtained from *in situ* Mott-Schottky analysis and photoelectrochemical studies) for passive films on pure metals, which shows that the dopants (donors for n-type semiconductors and acceptors for p-type semiconductors) are the defects themselves, including cation vacancies, anion vacancies, and cation interstitials.

In earlier work, much of the electrochemistry concerning iron was carried out in acid solutions. However, over the past thirty years, electrochemical studies on the passivity of iron have focused on neutral and alkaline buffer solutions. The impetus for work in neutral and alkaline solutions was from two papers by Nagayama and Cohen [3,4]. Their research was carried out in a sodium borate-boric acid buffer solution of pH 8.4. This pH value was chosen partly because the currents in both the active and passive regions were much less than those observed in acid solutions and hence led to much less roughening of the electrode surface. Although the passive film on iron formed in neutral and alkaline aqueous solutions has been extensively studied in the past [5-8], there is little consensus as to the electronic and

crystallographic properties of the passive film that forms on the metal surface. Some previous work [9] has shown that the passive film formed on iron in borate buffer solutions has a bilayer structure comprising a defective inner Fe_3O_4 layer and an outer γ-Fe_2O_3 layer. General agreement exists that the passivity of iron is primarily due to the barrier layer, although the outer layer that most likely forms by precipitation significantly modifies the electrochemical response of the interface as a whole.

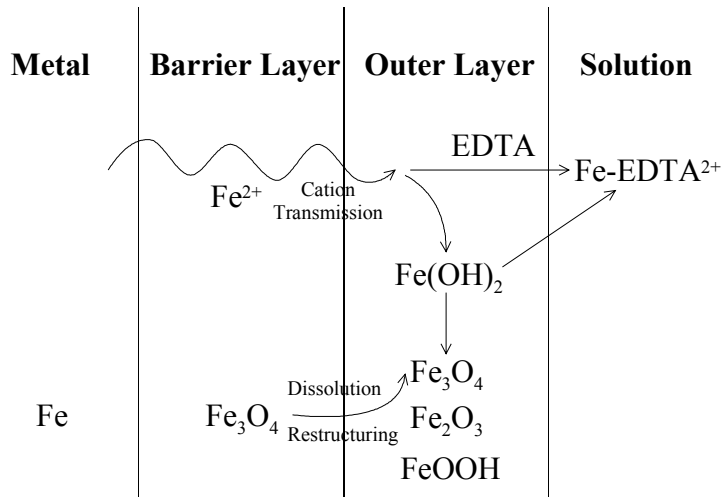

Figure 4.1. The structure of passive films formed on iron in borate buffer solutions with and without EDTA.

EDTA (Ethylene Diammine Tetraacetic Acid, disodium salt, $C_{10}H_{14}N_2Na_2O_8$) is extensively used as a chemical cleaning agent for the removal of iron oxide and other scales in steam raising plants, hot water circulating systems, etc [10]. EDTA is relatively stable under anodic polarization conditions, and its principal role is to chelate Fe^{2+} cations being released from the surface. It was shown by ellipsometry [11] that cathodic reduction and removal of the passive film on iron in a NaOH+EDTA solution occurred completely and rapidly. Also EDTA added to the alkaline electrolyte in iron batteries was found to increase their capacity [12], but the mechanism of this effect remains to be clarified. As mentioned above, the passivity of iron is associated with the formation of a three dimensional oxide film, which acts as a barrier between the metal and the electrolyte. A cartoon describing the interaction of EDTA with the passive film on iron is shown in Figure 4.1. The hypothesis upon which the present work is based is that EDTA, which chelates the iron cations that are ejected from the barrier layer, should be effective in preventing the formation of the outer layer. In that case, the barrier layer alone can be investigated to provide a more accurate account of its defect structure.

The Point Defect model (PDM) has been developed by Macdonald and his co-workers over the past twenty years to provide a mechanism-based description of the growth and breakdown of passive films [13,14]. This model has been used successfully to account for steady state and transient properties (including impedance characteristics) and the nucleation of localized corrosion due to passivity breakdown on many metals and alloys in contact with aqueous solutions [1,13]. The PDM provides an atomic scale description of the interfacial processes that lead to the generation and annihilation of defects that control the coupling between the electronic and crystallographic defect structures of the barrier film. In recent years, diagnostic criteria based on the PDM have been derived for investigating the electrical field-thickness relationship and the kinetics of oxide film growth, including the identification of the principal defects in the barrier layer [15].

In Part I of this series [16], the general electrochemical behavior of iron in borate buffer solution with and without EDTA being present in the system was explored. It was shown that EDTA inhibits the formation of the outer layer, presumably by complexing Fe^{2+} and/or Fe^{3+} that are ejected from the barrier layer and hence inhibits their hydrolysis and oxidation (Fe^{2+} only) to form a precipitate at the outer surface of the inner layer. In the present paper, potentiodynamic polarization and steady state techniques, including Mott-Schottky analysis, have been used to study the electrochemical properties of the passive film formed on iron in borate buffer solutions at ambient temperature and as a function of pH with and without the addition of EDTA. We also report transient studies that provide diagnostic information on the mechanism of growth of the barrier layer. The Point Defect Model (PDM) has been employed to interpret the mechanism of the interfacial charge transfer processes that lead to the steady state and transient behaviors of the passive film formed on iron.

4.3: EXPERIMENTAL

A polytetrafluoroethylene (PTFE) cell containing ports for three electrodes and for gas purging was used for the electrochemical studies. The working electrode was an iron rod (Alfa Aesar 99.99%) with a diameter of 1 mm (geometric area of $0.008 cm^2$). The electrode was sealed into a polyvinyl chloride (PVC) rod with cyanocrylate glue and two-component epoxy. The iron electrode was polished with LECO SiC paper from 600 grit to 1200 grit, and then with cotton cloth / 0.05µm Al_2O_3, which produced a smooth, bright ("mirror") surface, as observed microscopically. The counter electrode was a platinum wire of high purity (99.998%). A saturated calomel reference electrode (SCE) was located in a separate container which was connected to the cell via a salt bridge and Luggin probe. The borate buffer solutions were prepared from Aldrich A.C.S. reagents and conductivity grade water (Milli-Q system, 18.2 MΩ cm^{-1}). Table 4.1 displays the compositions of the solutions, together with the measured pH values as determined using a Fisher Scientific pH meter. Prior to and during all experiments, the electrolyte was purged with high purity ("zero-grade") nitrogen gas with an oxygen concentration of less than 1 ppm. All experiments were carried out at ambient temperature (~22°C). Potential and current control of the working electrode was achieved by using a Schlumberger/Solartron 1286 electrochemical interface, which was controlled by CorrWare for Windows (version 1.4) software. The capacitance of the interface was recorded with a Schlumberger/Solartron 1250 Frequency Response Analyzer using an excitation voltage of 10 mV (peak-to-peak), and an applied frequency of 1 kHz. To remove the air formed oxide film, the samples were cathodically polarized at -1V vs. SCE for 5 minutes prior to all experiments.

Table 4.1. Compositions and pH values of test solutions

Solution Name	Solution Compositions	Measured pH
bb8.4	0.3M H_3BO_3 + 0.075M $Na_2B_4O_7$	8.36
bb8.4+EDTA	0.3M H_3BO_3 + 0.075M $Na_2B_4O_7$ + 0.01M EDTA	8.27
bb9.2	0.05M H_3BO_3 + 0.075M $Na_2B_4O_7$	9.17
bb9.2+EDTA	0.05M H_3BO_3 + 0.075M $Na_2B_4O_7$ + 0.01M EDTA	9.07
bb10.0	0.075M NaOH + 0.075M $Na_2B_4O_7$	9.98
bb10.0+EDTA	0.075M NaOH + 0.075M $Na_2B_4O_7$ + 0.01M EDTA	9.80

4.4: RESULTS AND DISCUSSION

Figure 4.2 demonstrates that EDTA enhances the active dissolution current for iron in borate buffer solution of pH 8.4. It is also observed that the rate of the cathodic reaction is enhanced when EDTA is present, most likely due to removal of the outer layer of the passive film or possibly due to a change in the defect structure of the barrier layer that results in a higher exchange current density for the hydrogen electrode reaction. These findings agree with those that we reported in Part I [16]. Figure 4.3 also shows the effect of pH on the polarization behavior of iron in borate buffer solution containing 0.01M EDTA, which confirms that more alkaline solutions inhibit the active dissolution of iron and correspondingly improve passivity.

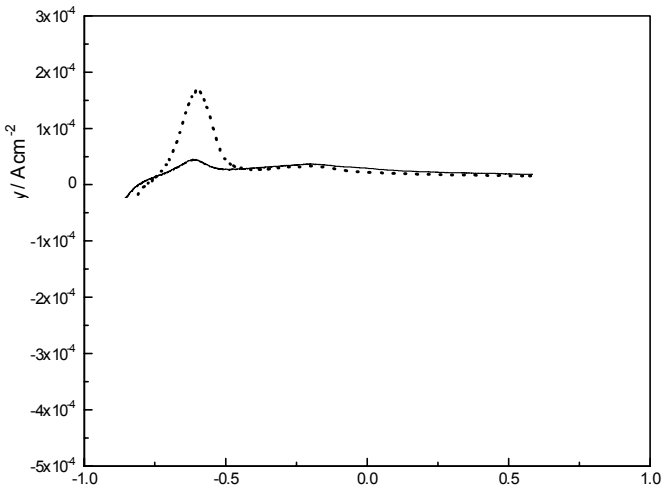

Figure 4.2. Polarization curves for iron in pH 8.4 borate buffer solution with (···) and without (—) 0.01 M EDTA. T= 22 ^{o}C, voltage sweep rate = 0.2 mV/s.

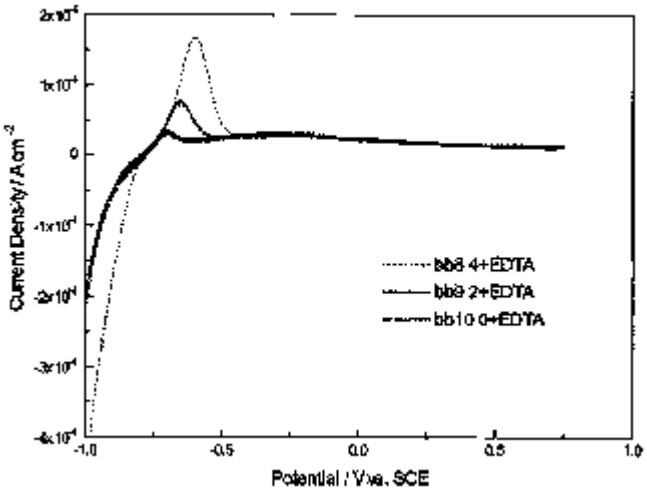

Figure 4.3. Polarization curves for iron in borate buffer solution with 0.01 M EDTA as a function of pH. T= 22 ^{o}C, voltage sweep rate = 0.2 mV/s.

Diagnostic criteria based on current transient data measured under potentiostatic (potential step) conditions have been employed to distinguish between the PDM (Point Defect Model) and the HFM (High Field Model) for describing the growth of oxide films (barrier layer on metals and alloys) [15]. According to the HFM, the transient in current in response to an imposed potential step should follow the expression

$$\sqrt{\frac{-i'}{i(i-\delta)}} = \left(\frac{1}{\chi F}\sqrt{\frac{\Omega RT}{a\Delta V}}\right)\ln i - \left(\frac{1}{\chi F}\sqrt{\frac{\Omega RT}{a\Delta V}}\right)\ln A \tag{1}$$

and hence a plot of $\sqrt{-i'/i(i-\delta)}$ [i.e., f (i)] vs. ln i should be linear with a positive slope. On the other hand, the PDM predicts that the current transient should obey

$$\sqrt{\frac{-i'}{i(i-\delta)}} = \sqrt{\frac{\alpha_3 \varepsilon \Omega}{RT}} \tag{2}$$

which means that $\sqrt{-i'/i(i-\delta)}$ is a constant and hence that a plot of $\sqrt{-i'/i(i-\delta)}$ vs. ln i should be a horizontal line. In these equations, i is the current density (A/cm^2), δ is the steady state current density (A/cm^2), i' is the differential di/dt, χ is the cation valence (8/3 on average or 2 or 3 for Fe_3O_4), F is Faraday's constant (96487 C/equiv), Ω is the molar volume per oxide cation (14.9 cm^3/mol), R is the gas constant (8.314 J/mol/K), T is the Kelvin temperature (~295K), a is the half-jump distance (assumed to be 1.5*10^{-8} cm), ΔV is the applied overpotential with respect to the equilibrium potential for the Fe/Fe_3O_4 couple under the prevailing conditions, A is a temperature -dependent constant, α_3 is the transfer coefficient for the generation of oxygen vacancies at the metal/film interface (0<α_3<1, assumed to be 0.5), and ε is the field strength within the barrier layer. The growth of the passive film on iron in pH 10.0 borate buffer solutions with and without EDTA shows that the PDM provides a better account of the experimental data than does the HFM, as is evident from the data presented in Figures 4.4 and 4.5.

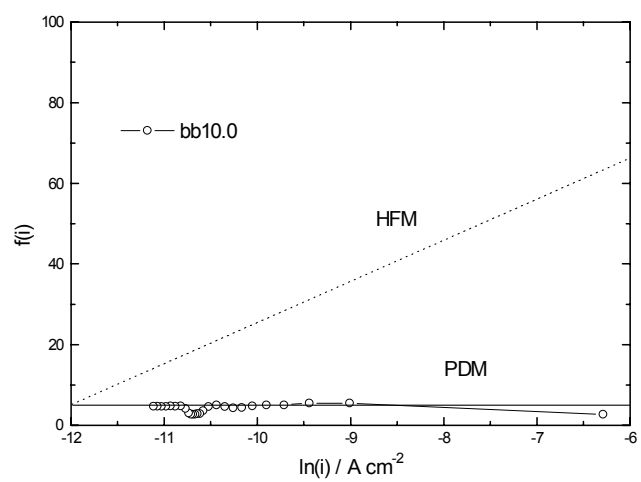

Figure 4.4. Diagnostic test for the growth mechanism for the passive film on iron in pH 10.0 borate buffer solution without 0.01 M EDTA at 22 ^{o}C. A horizontal line indicates that the growth mechanism is the Point Defect Model whereas a line with the indicated slope indicates the high field mechanism.

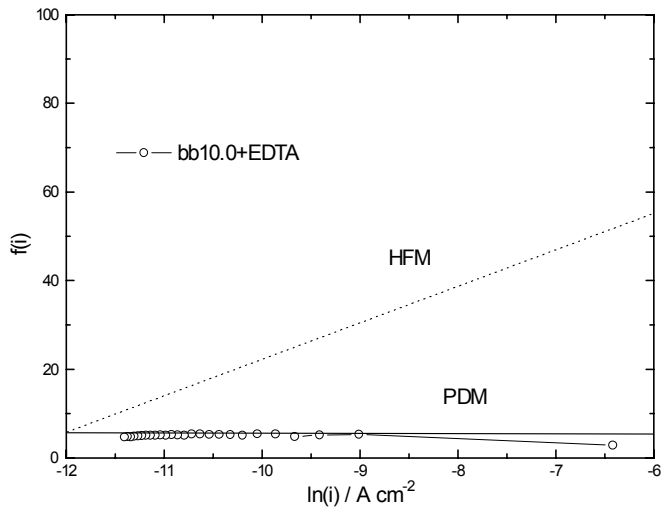

Figure 4.5. Diagnostic test for the growth mechanism for the passive film on iron in pH 10.0 borate buffer solution with 0.01 M EDTA at 22 ^{o}C. A horizontal line indicates that the growth mechanism is the Point Defect Model whereas a line with the indicated slope indicates the high field mechanism.

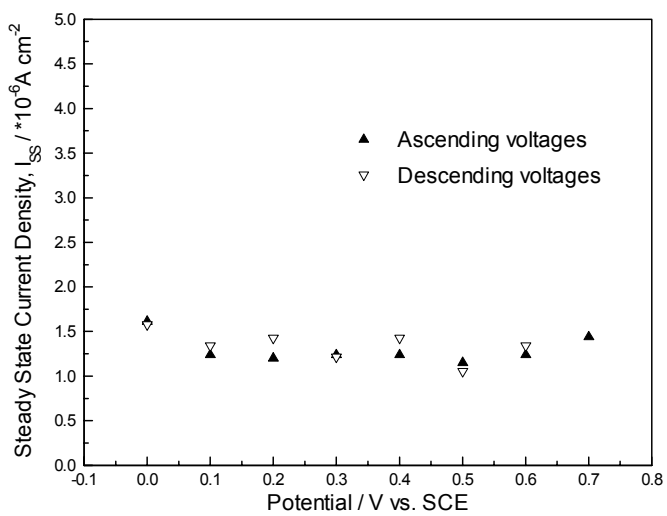

Figure 4.6. Plots of steady state current density as a function of applied voltage for iron in pH 10.0 borate buffer solution with 0.01M EDTA at 22 ± 2 ^{o}C. "Up" means changing the potential in the negative-to-positive direction; "down" in the positive-to-negative direction.

The PDM, which allows for the existence of a steady state current, in contrast to the HFM, also accounts for a dependence of the steady state passive current on the applied potential.

Using this dependence, a number of diagnostic criteria have been developed [1,13] to identify the principal crystallographic and electronic defects, on the basis that the passive film is a defect semiconductor. For example, it is clearly shown in Figure 4.6 that the steady state current density (each point being measured after 24 hours of polarization in the ascending and descending potential directions) for passive iron in pH 10.0 borate buffer solution with 0.01M EDTA does not depend on the applied potential, which is diagnostic of the principal defects being oxygen vacancies and/or iron interstitials. This is consistent with the well-known n-type character of the passive film on iron shown in our previous work, as determined by Mott-Schottky analysis [16] and photoelectrochemical techniques [2].

The film thickness can be estimated from capacitance data using the well-known "parallel plate" expression, as

$$L_{SS} = \frac{\hat{\varepsilon}\varepsilon_0 A}{C} \tag{3}$$

provided all other series capacitances are large compared with that of the film. In this expression, L_{SS} is the steady state thickness, C is the capacitance (F), A is the surface area of the electrode (cm^2), ε_0 is the vacuum permittivity (8.85×10^{-14} F cm^{-1}), and $\hat{\varepsilon}$ is the dielectric constant. The dielectric constant of 30 was established by requiring L_{SS} to extrapolate to the equilibrium potential for Fe/Fe_3O_4, as required by the PDM. Figure 4.7 shows the dependence of the passive film thickness on iron in pH 8.4 borate buffer solutions with and without 0.01M EDTA on the applied potential. The linear increase in the thickness with formation potential agrees with the diagnostic criteria for barrier passive films, according to the PDM. The plots in Figure 4.7 clearly show that when EDTA is present, the passive film on iron is thinner compared with that without EDTA, presumably because EDTA removes the outer layer and enhances the rate of dissolution of the barrier layer.

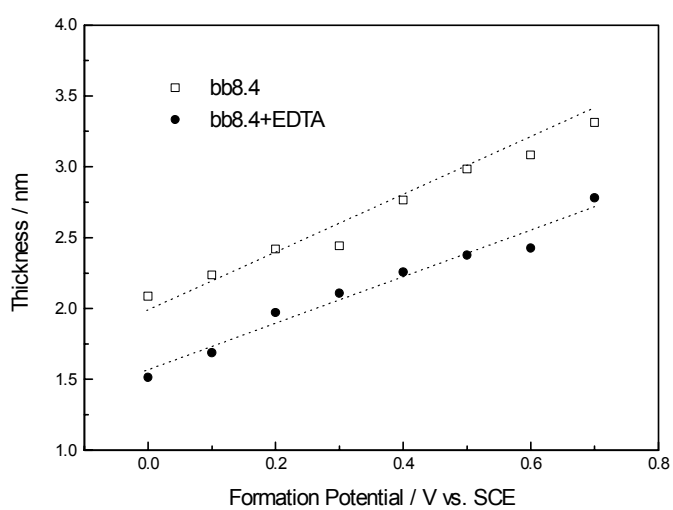

Figure 4.7. Plots of steady state film thickness as a function of applied voltage for iron in pH 8.4 borate buffer solution with and without 0.01M EDTA at 22 ± 2 ^{o}C.

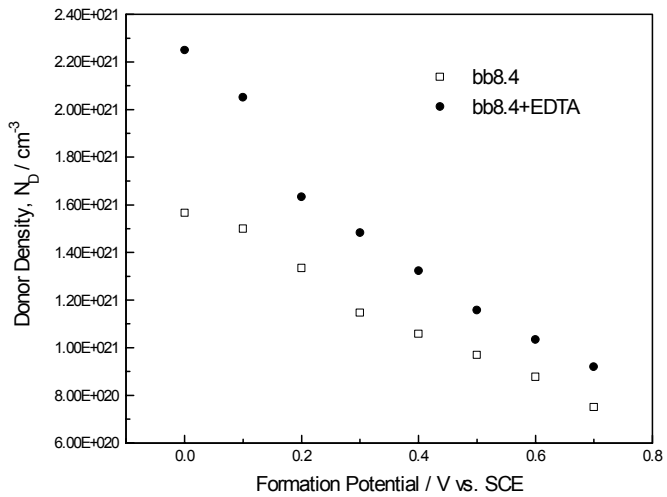

Figure 4.8. Plots of donor density as a function of formation voltage for iron in pH 8.4 borate buffer solution with and without 0.01 M EDTA at 22 ± 2 ^{o}C.

Mott-Schottky analysis is an important, *in situ* method for probing the semiconducting properties of passive films. The Mott-Schottky plots for passive iron obtained in the present work are characteristic of those for an n-type semiconductor. No p-type character was detected at any potential within the passive range. The capacitance data were measured while sweeping the potential in the negative direction from the formation voltage (at which the system existed in the steady state) at a sufficiently high sweep rate that the barrier layer thickness remains constant. It has been previously argued [2] that a constant film thickness condition more closely approximates the conditions assumed in deriving the Mott-Schottky expression. Donor density vs. formation potential data have been calculated from the Mott-Schottky plots for passive films formed on iron in pH = 8.4 borate buffer solutions with and without 0.01M EDTA (Figure 4.8). The data plotted in these figures show that the donor density in the passive film (close to the metal/film interface) decreases with increasing formation potential, which is in agreement with the prediction of the PDM (Point Defect Model). The donor density shown in Figure 4.8 indicates that the passive film formed on iron in borate buffer solution with EDTA is more defective than that formed in the absence of EDTA. This phenomenon may result from the lower thickness of the passive film formed in borate buffer solution with EDTA and hence may account for the enhanced rate of hydrogen evolution. With regard to the latter, and assuming that the exchange current density for the hydrogen electrode reaction (her) is governed by quantum mechanical tunneling of charge carriers (electrons) from defect-to-defect across the barrier layer (indirect tunneling), the higher defect concentration in the barrier layer formed in the presence of EDTA accounts for the higher hydrogen evolution rate at a given potential (Figure 4.2).

Some passivity models have been developed to make analytical predictions with respect to the response of the film thickness and current upon common independent variables (potential, pH). Verwey's model [17] is applicable to cation conductors, in which cation motion in the oxide passive film is the rate controlling step, while Cabrera-Mott's model [18] (also for cation conductors) regards cation injection from metal into film as the rate control step. In both of these models, the film grows at the film/solution interface and hence it is not obvious how the models can account for the commonly observed bilayer structure. Both of these models predict transient changes of current density and film thickness with time, but neither predicts the existence of

steady states in these properties at finite times. Vetter and Gorn [19] developed a model for the passive film on iron that recognized the existence of potential drops across the interfaces. However, this model makes predictions only with respect to the transient current behavior. The place exchange model [20] postulates cooperative cation/anion exchange and injection of oxygen ion into the film as the rate-determining steps. The model predicts transient current density and film thickness behavior, but it does not account for the steady state. Kirchheim's model [21] for passive iron under potentiostatic conditions combines the high field transport through the passive film with the transport through the film-electrolyte interface, and proposes that the electric field strength within the passive film is unconstrained, contrary to our experimental findings of a voltage-independent electric field within the passive film (Figure 4.4, 4.5 and 4.7). According to the Point Defect Model (PDM) [13], the occurrence of band-to-band (Esaki) tunneling is postulated to produce a counter field that buffers the applied field; the field strength must therefore be limited in its upper value, i.e., the field strength is constrained. Unlike the High Field Models (HFMs), such as Verwey's model [17] and Cabrera-Mott's model [18], the PDM incorporates film dissolution and interfacial potential differences in describing the electronic structure of the passive film in terms of highly doped, defect semiconductor concepts. The PDM is perfectly general, in that it is applicable to cation/interstitial/anion conductors and predicts the steady state and transient behaviors of film thickness and current density, the impedance characteristics, alloy segregation, and passivity breakdown [1]. The rate-determining step in the PDM is considered to be the injection of positive charge in the form of oxygen vacancies ($V_O^{\cdot\cdot}$), metal cations ($M^{\chi+}$), or metal interstitials ($M_i^{\chi+}$) into the film at the metal/film interface, but under conditions where the potential drop across the barrier layer and not the field changes with time as the film thickens or thins.

The Point Defect Model [1,2,13], as applied to iron, is shown schematically in Figure 4.9. Reaction (1) describes the consumption of cation vacancies at the metal/film interface that are produced by Reaction (4) at the film/solution interface. Reaction (2) is responsible for the injection of iron interstitials ($Fe_i^{\chi+}$) into the barrier layer, while the ejection of metal interstitials at the barrier layer/solution interface is described by Reaction (5). Reaction (3) leads to the growth of the barrier layer into the metal, and Reaction (7) results in the destruction of the barrier layer by dissolution. Reaction (6) describes oxygen vacancy annihilation at the film/solution interface and hence injection of oxygen ions into the film. Note that Reactions (1), (2), (4), (5), and (6) are lattice conservative processes, in that they do not result in movement of the respective interfaces, whereas Reactions (3) and (7) are not. The steady state must involve a balance in the rates of the two nonconservative Reactions (3) and (7), since only one nonconservative reaction would lead to monotonic growth or thinning of the passive film. Classification of the reactions as to whether they are lattice conservative or non-conservative is a critical feature of the PDM, and it is one that sets this model apart from other models that have been proposed for the passive state.

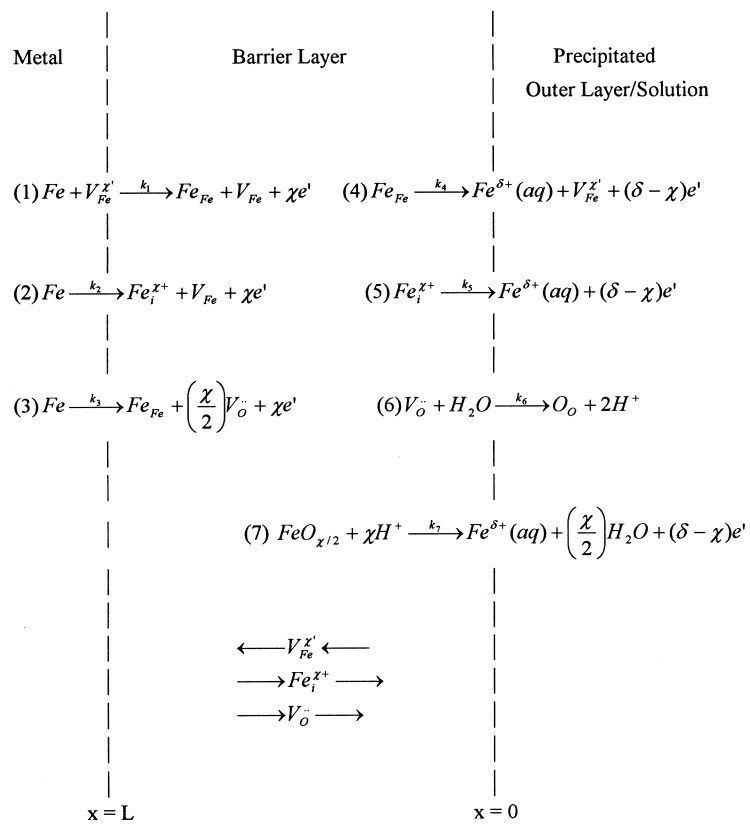

Figure 4.9. Summary of the defect generation and annihilation reactions occurring at the interfaces of the barrier oxide layer on passive iron according to the Point Defect Model. $Fe \equiv$ iron atom, $V_{Fe}^{\chi'} \equiv$ iron vacancy, $Fe_i^{\chi+} \equiv$ iron interstitial, $V_{\ddot{O}} \equiv$ oxygen vacancy, $Fe^{\delta+}(aq) \equiv$ iron cation in outer layer/solution, $Fe_{Fe} \equiv$ iron cation in cation site on the cation sublattice, $O_O \equiv$ oxygen ion in anion site on the anion sublattice, $FeO_{\chi/2} \equiv$ stoichiometric barrier layer oxide.

The steady state thickness (L_{SS}) is derived as [1,13]

$$L_{SS} = \left[\frac{1-\alpha}{\varepsilon} - \frac{\alpha\alpha_7(\delta-\chi)}{\alpha_3\chi\varepsilon}\right]V + \frac{1}{\alpha_3\chi\varepsilon}\left[\frac{2.303n}{\gamma} - \beta(\alpha_7\delta - \alpha_7\chi + \alpha_3\chi)\right]pH + \frac{6.909n}{\alpha_3\chi\gamma\varepsilon} - \frac{\alpha_7\delta - \alpha_7\chi + \alpha_3\chi}{\alpha_3\chi\varepsilon}\phi_{f/s}^0 + \frac{1}{\alpha_3\chi\gamma\varepsilon}\ln\left(\frac{k_3^{0\,\prime}}{k_7^{0\,\prime}}\right) \tag{4}$$

and the steady state current density (I_{SS}) is given by

$$I_{SS} = \delta F\left[k_4^0 e^{\alpha_4\alpha\delta\gamma V} + k_2^0 e^{\alpha_2(1-\alpha)\chi\gamma V} e^{-\alpha_2\chi K L_{SS}} + k_3^0 e^{\alpha_3(1-\alpha)\chi\gamma V} e^{-\alpha_3\chi K L_{SS}}\right] \tag{5}$$

where ε is the electric field strength, V is the applied potential, α_j, k_j^0 and $k_j^{0\,\prime}$ are the transfer coefficient, the rate constant, and the standard rate constant, respectively, for the jth interfacial

reaction, n is the kinetic order of the film dissolution reaction with respect to C_{H^+} at the barrier layer / solution interface, C_{H^+} is the hydrogen ion concentration in the solution at the barrier layer / solution interface, $\phi^0_{f/s}$ is the standard potential difference at the barrier layer / solution interface, $K = \varepsilon F / RT$, $\gamma = F / RT$, and α, β are constants. The diagnostic criteria for the passive films according to the PDM are presented in Table 4.2 [22].

Table 4.2. Diagnostic criteria for passivity in terms of the PDM

Conduction Mechanism	Electronic Defect Type	$\left(\frac{\partial L_{SS}}{\partial V}\right)_{pH,C_M}$	$\left(\frac{\partial L_{SS}}{\partial pH}\right)_{V,C_M}$	$\left(\frac{\partial \ln I_{SS}}{\partial V}\right)_{pH,C_M}$	$\left(\frac{\partial \ln I_{SS}}{\partial pH}\right)_{V,C_M}$	Example
Anion Vacancy	n	constant >0	constant >0 or <0	0	constant >0 or <0	W
Cation Interstitial	n	constant >0	constant >0 or <0	0	constant >0 or <0	Zn
Cation Vacancy	p	constant >0	constant >0 or <0	constant >0	constant >0 or <0	Ni

The diagnostic criteria when applied to the data obtained in this study show that the passive film on iron is an n-type semiconductor, due to a preponderance of oxygen vacancies and/or iron interstitials. Recent, *in situ* X-ray diffraction studies by Toney, et. al. [23, 24] concluded that the passive film on iron is a "highly defective spinel oxide with cation vacancies on octahedral and tetrahedral sites (80±10% and 66±10% occupancies, respectively) and with cations occupying octahedral interstitial sites (12±4% occupancy)". However, cation vacancies cannot contribute significantly to the electronic structure of the passive film on iron, because they should impart p-type character. From the present work, we conclude that the dominant defects must be oxygen vacancies, which are generated by growth of the barrier layer into the metal (Reaction 3, Figure 4.9), and/or cation (Fe^{2+} or possibly Fe^{3+}) interstitials, because of the n-type electronic character of the film.

4.5: SUMMARY AND CONCLUSIONS

Characterization of the passive state on iron in borate buffer solutions over a narrow range of pH (8.4 – 10) with and without 0.01M EDTA is reported. It was found that EDTA present in borate buffer solution effectively suppresses the formation of the outer layer, and therefore allows the barrier layer to be studied alone. Passivation is enhanced by higher pH values of the solution. The PDM (Point Defect Model), not the HFM (High Field Model), gives a better account of the kinetics of film growth. Furthermore, steady state polarization data show that the passive film on iron is an n-type semiconductor, due to a preponderance of oxygen vacancies and/or iron interstitials. Mott-Schottky analysis further confirms that the passive film formed on iron is an n-type semiconductor. The donor density of the barrier layer decreases and the steady state thickness increases linearly with increasing film formation potential, in agreement with the predictions of the PDM.

4.6: REFERENCES

1. D. D. Macdonald, *Pure Appl.Chem.*, **71** (1999) 951.
2. D. D. Macdonald, S. R. Biaggio and H. Song, *J. Electrochem. Soc*., **139** (1992) 170.
3. M. Nagayama and M. Cohen, *J. Electrochem. Soc*., **109** (1962) 781.
4. M. Nagayama and M. Cohen, *J. Electrochem. Soc*., **110** (1963) 670.
5. N. Sato, T. Noda and K. Kudo, *Electrochim. Acta,* **19** (1974) 471.
6. B. D. Cahan and C.T. Chen, *J. Electrochem. Soc.,* **129** (1982) 474.
7. J. Kruger, *Corr. Sci.,* **29** (1989) 149.
8. P. Schmuki, S. Virtanen, A. Davenport and C. Vitus, *J. Electrochem. Soc.,* **143,** (1996) 574.
9. M. Büchler, P. Schmuki, H. Böhni, T. Stenberg and T. Mäntylä, *J. Electrochem. Soc.,* **145** (1998) 378.
10. D. A. Frey, *Mater. Perform*., **20** (1981) 49.
11. Z. Szklarska-Smialowska, T. Zakroczymski and C. J. Fan, *J. Electrochem. Soc.*, **132,** (1985) 2543.
12. T. Yabumoto and K. Ohsawa, *Jpn. Kokai*, **75**, 45, 243.
13. D. D. Macdonald, *J. Electrochem. Soc*., **139** (1992) 3434.
14. C. Y. Chao, L. F. Lin and D. D. Macdonald, *J. Electrochem. Soc*., **128** (1981) 1187.
15. L. Zhang, D. D. Macdonald, E. Sikora and J. Sikora, *J. Electrochem. Soc.*, **145** (1998) 898.
16. E. Sikora and D. D. Macdonald, *J. Electrochem. Soc*., in press (2000).
17. E. J. W. Vervey, *Physica,* **2** (1935) 1059.
18. N. Cabrera and N. F. Mott, *Report Progr. Phys.*, **12** (1948) 163.
19. K. J. Vetter and F. Gorn, *Electrochim. Acta,* **18** (1973) 321.
20. N. Sato and M. Cohen, *J. Electrochem. Soc.,* **111** (1964) 512.
21. R. Kirchheim, *Electrochim. Acta,* **32** (1987) 1619.
22. D. D. Macdonald, K. M. Ismail and E. Sikora, *J. Electrochem. Soc.* , **145** (1998) 3141.
23. M. F. Toney, *Physical Review Letters,* **79**, 21 (1997) 4282.
24. J. Davenport, L. J. Oblonsky, M. P. Ryan and M. F. Toney, *J. Electrochem. Soc.* , **147** (2000) 2162.

CHAPTER 5

PUBLICATIONS AND STUDENT THESES

5.1: PUBLICATIONS IN PEER REVIEWED JOURNALS

1. Cho, E., H. Kwon, and D. D. Macdonald, "Study of the Passive Film Formed on Fe-20Cr by Photocurrent and Mott-Schottky Analyses", Corros. Sci., submitted (2001).
2. Vankeerberghen, M., and D. D. Macdonald, "Predicting Crack Growth Rate vs. Temperature-Behaviour of Type 304 Stainless Steel in Dilute Sulfuric Acid Solutions", Corros. Sci., in press (2002).
3. Macdonald, D. D., M. Al-Rafaie and G. R. Engelhardt, "New Rate Laws for the Growth and Reduction of Passive Films", J. Electrochem. Soc., **148**(9), B343 - B347 (2001).
4. Liu, J. and D. D. Macdonald, "The Passivity of Iron in EDTA-Containing Solutions. Part II: Nature of the Passive Film", J. Electrochem. Soc., **148**(11), B425-B430 (2001).
5. Macdonald, D. D., "Theoretical Interpretation of Anion Size Effects in Passivity Breakdown", Proc. Electrochem. Soc., Vol. **2000-25**, 141-154 (2001).
6. Gomez_Duran, M. and D. D. Macdonald, "Stress Corrosion Cracking of Type 304 SS in Thiosulfate Solution", Corros. Sci., submitted (2002).
7. Sikora, E. and D. D. Macdonald, "Nature of the Passive Film on Nickel", Electrochim. Acta, submitted (2002).

5.2: PUBLICATIONS IN CONFERENCE PROCEEDINGS

1. Macdonald, D. D., "Theoretical Interpretation of Anion Size Effects in Passivity Breakdown", Proc. Electrochem. Soc., Vol. **2000-2**, Abstr. 405 (Oct 22-27, 2000, Phoenix, AZ).
2. Urquidi-Macdonald, M. and D. D. Macdonald, Transients in the Growth of Passive Films on High Level Nuclear Waste Canisters", Proc. Int. Workshop Pred. Long Term Corros. Behav. Nucl. Waste Systs., (Commissariat a l'Energie Atomique and Pennsylvania State University), Cadarache, France, Nov. 26-29 (2001), in press.
3. Macdonald, D. D., "The Role of Internal/External Environment Coupling in Stress Corrosion Cracking", in Chemistry and Electrochemistry of Stress Corrosion Cracking: A Symposium Honoring the Contributions of R. W. Staehle", (Ed. R. H. Jones), TMS (The Minerals, Metals, and Materials Soc), 2001, pp 193-210.
4. Macdonald, D., Engelhardt, G. "Towards a Mechanism Based Theory for Crack Initiation," CORROSION 2001 (NACE International, Houston, TX), Paper, (2001).
5. Aligizaki K.K., and D. D. Macdonald, "Diagnostic Analysis of the Growth of Passive Films on Aluminum," Proceedings of Symposium E1: Corrosion and Corrosion Prevention of Low Density Metals and Alloys, Eds B. A. Shaw, R. G. Buchheit, and J. P. Moran, Vol. **2000-23**, Electrochemical Society 198th Meeting, Phoenix, AZ, October 22-27, 2000, pp 211-219.

6. Liu, S. and D. D. Macdonald, "Fracture of AISI 4340 Steel in Concentrated Sodium Hydroxide Solution", CORROSION/2001 (NACE Int., Houston, TX), Paper **01236**, 15 pp, (2001).
7. Macdonald, D. D., "Deterministic Prediction of Localized Corrosion Damage", Proc.12th Asia-Pacific Corros. Control Conf., (Seoul, Korea, Oct. 8-12,2001), **1**, 67-81 (2001).

5.3: STUDENT'S THESES

Monika Gomez-Duran, "Determination of the Fate of the Current Generated During Stress Corrosion Cracking of Sensitized Type 304 Stainless Steel in Thiosulfate Solution", MS Thesis, Pennsylvania State University, 2001.